

MICROCOPY RESOLUTION TEST CHART  
NATIONAL BUREAU OF STANDARDS-1963-A

UNCLASSIFIED

(4)

SECURITY CLASSIFICATION OF THIS PAGE (When Data Entered)

REPORT DOCUMENTATION PAGE		READ INSTRUCTIONS BEFORE COMPLETING FORM
1. REPORT NUMBER <b>AFOSR-TR- 83-0346</b>	2. GOVT ACCESSION NO. <b>AD-A127786</b>	3. RECIPIENT'S CATALOG NUMBER
4. TITLE (and Subtitle) <b>Research Progress and Forecast Report for MSNW FEL Oscillator Program</b>		5. TYPE OF REPORT & PERIOD COVERED <b>Annual Report (6/15/81-8/14/82)</b>
		6. PERFORMING ORG. REPORT NUMBER <b>C.11.198.01</b>
7. AUTHOR(s) <b>J. Slater, D.C. Quimby, W. Grossman</b>		8. CONTRACT OR GRANT NUMBER(s) <b>F49620-81-C-0079</b>
		10. PROGRAM ELEMENT, PROJECT, TASK AREA & WORK UNIT NUMBERS <b>61102F 2301/A1</b>
9. PERFORMING ORGANIZATION NAME AND ADDRESS <b>Mathematical Sciences Northwest, Inc. 2755 Northup Way Bellevue, WA 98004</b>		11. CONTROLLING OFFICE NAME AND ADDRESS <b>USAF, AFSC Air Force Office of Scientific Research Bldg. 410, Bolling AFB DC 20332</b>
		12. REPORT DATE <b>January 1983</b>
14. MONITORING AGENCY NAME & ADDRESS (if different from Controlling Office)		13. NUMBER OF PAGES <b>60</b>
		15. SECURITY CLASS. (of this report) <b>Unclassified</b>
16. DISTRIBUTION STATEMENT (of this report)  <b>Approved for public release; distribution unlimited.</b>		15a. DECLASSIFICATION/DOWNGRADING SCHEDULE
17. DISTRIBUTION STATEMENT (of the abstract entered in Block 20, if different from Report)		
18. SUPPLEMENTARY NOTES		
19. KEY WORDS (Continue on reverse side if necessary and identify by block number) <b>Free-electron laser, oscillator, mode structure, mode control, diffraction</b>		
20. ABSTRACT (Continue on reverse side if necessary and identify by block number) <b>The purpose of this program is to provide assessment data for determining the potential of tapered-wiggler free-electron laser (FEL) oscillators. It is expected that the tapered-wiggler concept will lead to the development of high-efficiency FELs by providing substantial energy extraction in a single pass of the e-beam through the wiggler magnet. The work consists of parallel theory and experimental tasks. The latter involve parameterization of the FEL interaction on a single-</b> (cont.)		

AD A 127786

DTIC  
SELECTED  
MAY 9 1983  
A

DTIC FILE COPY

DD FORM 1473 1 JAN 73

EDITION OF 1 NOV 65 IS OBSOLETE

83 05 06 - 182

UNCLASSIFIED

SECURITY CLASSIFICATION OF THIS PAGE (When Data Entered)

UNCLASSIFIED

SECURITY CLASSIFICATION OF THIS PAGE(When Data Entered)

20. pass basis, and this portion of the work has not yet been completed. The theory work described here deals with the transverse mode structure of FEL oscillators. This mode analysis has shown that
- 1) the one-way nature of the FEL gain media results in an asymmetric mode which is not an eigenmode of the cavity, i.e., it is described as a linear combination of cavity modes,
  - 2) the higher-order mode content is largest in confocal or concentric cavities, rather than the intermediate cases,
  - 3) the higher-order mode content can be controlled by aperturing, and
  - 4) the quality of the output beam is nearly diffraction limited.

UNCLASSIFIED

SECURITY CLASSIFICATION OF THIS PAGE(When Data Entered)

MSNW C.11.198.01

RESEARCH PROGRESS AND FORECAST REPORT FOR  
MSNW FEL OSCILLATOR PROGRAM

Annual Report  
(June 15, 1981 - August 14, 1982)

Submitted to

Air Force Office of Scientific Research

AOSR Contract Number F49620-81-C-0079

by

J. Slater, D. Quinby, and W. Grossman

MATHEMATICAL SCIENCES NORTHWEST, INC.

2755 Northup Way  
Bellevue, Washington 98004

January 1983



Accession For	
NTIS GRA&I	<input checked="" type="checkbox"/>
DTIC TAB	<input checked="" type="checkbox"/>
Unannounced	<input type="checkbox"/>
Justification	
R...	
Distribution/	
Availability Codes	
Dist	Avail and/or Special
A	

Approved for public release;  
distribution unlimited.

**Research Progress and Forecast Report  
for the MSNW FEL Oscillator Program**

The basic goal of this program is to provide assessment data for assessing the potential of tapered-wiggler FEL oscillators. The advantage of the tapered wiggler FEL, as compared to the original fixed pitch device demonstrated at Stanford, is that of high electron kinetic energy extraction in a single pass. It is expected that the tapered wiggler concept will lead to development of high efficiency free-electron lasers by reducing the need for electron beam recirculation or recovery.

The fact that large deceleration of electrons could be achieved with a tapered-wiggler design was first demonstrated in the MSNW/BAC program, and since then MSNW/BAC and LANL have measured a net deceleration of several percent in separate experiments. To date, no oscillator experiment has been attempted. This AFOSR program is directed toward bridging the gap between the current single pass measurements and future oscillator work. It embodies complementary experimental and theoretical tasks which are intended to assess oscillator potential in the near term using single pass data. The AFOSR experimental tasks require use of the MSNW/BAC facility developed under DARPA sponsorship, and it is necessary that a subset of the DARPA experiments be largely successful before the AFOSR sponsored work can begin. In particular, the DARPA high extraction experiment must run in a sufficiently controllable way that parametric measurements can be made. Obtaining these parametric measurements is the experimental goal of this AFOSR program. The DARPA experiments have not yet advanced to the stage where such parameterization measurements would be meaningful, but the experiment is close to that point. In contrast, excellent progress and gain in understanding has already been made in the AFOSR theory task. The status of the experiment is described briefly below, and more detail is included in Appendix A.

APPENDIX A: PARAMETERIZATION  
NOTICE OF TRANSMITTAL TO DTIC  
This technical report has been reviewed and is approved for release under E.O. 11652-12.  
Distribution is unlimited.  
MATTHEW J. KEMNER  
1 Chief, Technical Information Division

analysis of the FEL emittance, a topic related to the present experimental difficulties, is given in Appendix B. A summary of theory results is presented below, and given in much greater depth in Appendix C.

### Experiment

The experimental tasks involve parameterization of the FEL interaction in terms of parameters useful to oscillator calculations, particularly start-up physics. In principle, measurement of the variation of the FEL interaction with respect to photon intensity and photon wavelength is needed. The wavelength sensitivity is necessary because of an expected tendency of tapered-wiggler devices to chirp during start-up, and it is actually to be measured not by variation of wavelength, but variation of the electron energy. The interaction can be measured in terms of either the net electron energy loss or equivalently the photon gain. The energy loss has been measured routinely as part of the DARPA program, and the capability to measure gain will be in place in early 1983. Measurement of the interaction at both high and low photon intensities is possible using a combination of techniques, with extraction measured at high CO<sub>2</sub> flux and gain measured at low CO<sub>2</sub> flux. Variation of the interaction as a function of e-beam energy, at any flux level, will be a relatively simple measurement once the system is operating properly. This measurement is made routinely now at high flux levels.

The main delay in the experiment has been achievement of e-beam extraction which is highly reproducible and in agreement with expectations, so that a parametric analysis is both possible and meaningful. The experiment has thus far achieved a net extraction of 2.5 percent, compared with an expected value of 4 percent. The difference lies in an overlap problem, which is apparently caused by excessive e-beam emittance and results in the electron beam exceeding the size of the photon beam. The emittance is only marginally excessive, and as a consequence, the results are quite sensitive to the tune of the Linac, and to adjustment of the e-beam transport system, both with respect to the

focal properties of the e-beam and its alignment relative to the wiggler's magnetic axis. Fluorescent screen diagnostics have recently been added to the wiggler so that the problem could be studied in detail. Coarse measurement of the emittance has been made with these measurements, along with an emittance acceptance analysis (Appendix B), indicating that the results are probably emittance limited. As a consequence, adjustment of the transport system will not solve the problem, but improvement should be attainable if emittance filtering is used. An extensive effort is in progress now to provide a small emittance beam by filtering, so that the maximum extraction can be obtained. Under these conditions the system will be comparatively insensitive to alignment and results therefore more repeatable. Parameterization measurements can then be started. It is expected that the emittance problem will be solved by early 1983.

The DARPA program has been modified from the original expectations in a way that affects the APOSR program. Originally, it was anticipated that a  $10\mu$  oscillator experiment would be included and that no single pass gain diagnostics would be developed. Now, the  $10\mu$  oscillator experiment has been eliminated (possibly to be replaced by a  $1\mu$  oscillator experiment in 1983) but development of a gain diagnostic for single-pass measurements at  $10\mu$  has been added. This allows additional capability in the APOSR program, for parametric studies, since these measurements can then be made at photon flux levels too small for measurable extraction.

### Theory

A study of oscillator transverse mode structure has been quite productive. The analysis is highly relevant to the current state of FEL technology, particularly in view of the oscillator design considerations underway at MSNW and LANL. Basically, the code developed is a numerical solution of Maxwell's equations for cylindrically symmetric geometries. It allows one to follow development of the mode structure of the tapered-wiggler oscillator, starting with an initial injected wave at saturation intensity. This injected wave develops over many round trips

of the optical cavity according to the influence of the FEL interaction, diffraction, and interaction with other elements of the optical cavity. Of particular interest is the effect of apertures on the mode structure, especially those associated with the wiggler magnets. Optimization studies have shown that the minimum wiggler bore, consistent with acceptable distortion due to clipping, yields the largest FEL interaction. The use of an injected wave may seem artificial, but at present it appears that injection may be required to achieve start-up in a reasonable time.

Evolving phase and amplitude profiles of the optical beam are calculated by direct integration of Maxwell's equations with the electrons providing the driving term. A convenient tool for understanding this evolution is the projection of the optical wave into normal modes of the optical cavity. That is, the fraction of total optical power in any particular cavity mode can be observed as a function of the round-trip number. One sees, for example, that a pure  $TEM_{00}$  wave injected into the optical cavity at the start of the calculation evolves an appreciable fraction of  $TEM_{10}$  mode over the course of several round-trips. This mode mixing is caused primarily by the nonuniform gain medium, and to a lesser extent, by the presence of the wiggler entrance and exit apertures. The primary findings, based on the resulting partition of energy among various cavity modes, are as follows:

1. The FEL interaction tends to produce an optical mode which is different from the injected wave and not an eigenmode of the cavity, meaning that the mode evolved is described by a combination of several cavity modes.
2. The fraction of higher order modes evolving can be controlled by aperturing.
3. Higher order mode content is especially evident in confocal cavities (those with mirror separation equal to the radius of

curvature) and concentric cavities (those with mirror separation equal to twice the radius of curvature).

4. Output quality of the oscillator is of nearly diffraction limited quality. This seemingly contradicts the finding that higher order modes are present, but in reality these modes are an indication of mode mismatch within the cavity, rather than a loss of quality. Details of the mode analysis are included in Appendix C.

Additional theoretical work is underway. We are preparing a 3-D code which will be used for mode analysis similar to that of the existing 2-D code, but additional important effects such as misalignment can be included. Tolerance to cavity misalignment is generally studied with geometrical optics codes, but the low Fresnel number FEL cavities are dominated by diffraction and one may find that the alignment tolerances do not follow conventional rules based on ray tracing. In addition, the 3-D code provides for analysis of complex cavities, such as those employing glancing incidence mirrors intended for use at high average power.

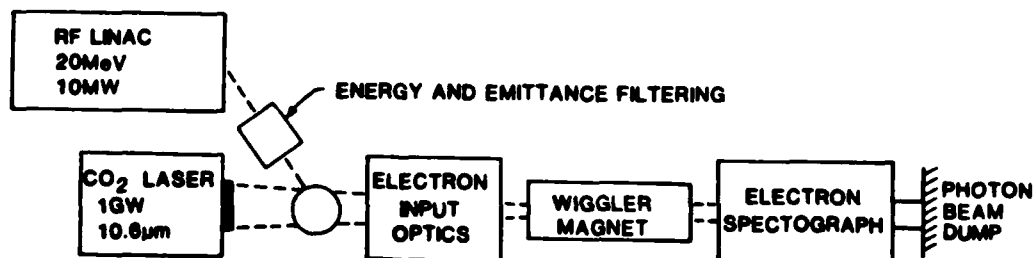
## APPENDIX A

### Summary of the MSNW/BAC Tapered Wiggler Verification Experiment

#### I. INTRODUCTION

The tapered-wiggler FEL concept may lead to development of a high efficiency, tunable laser. The tapered<sup>1</sup> version differs from the first FEL, which was demonstrated<sup>2</sup> at Stanford University, in that the resonant electron energy varies along the wiggler length so that resonant interaction is maintained as electrons decelerate. This resonant energy change results from variation of the wiggler magnetic field wavelength or amplitude as a function of axial position. Electrons trapped in the ponderomotive potential well, formed by the E-field of the photons and B-field of the wiggler, decelerate in accordance with the resonant energy change, or taper, of the wiggler. This can result in an electron kinetic energy loss far in excess of that permitted at a given photon flux for the constant pitch wiggler. The tapered-wiggler concept may lead to the development of high efficiency systems through reduction of e-beam energy recovery or recirculation requirements. Reported here are the initial results of tapered-wiggler verification experiments performed by Mathematical Sciences Northwest, Inc. in cooperation with the Boeing Aerospace Company.

Electron energy loss is measured in an amplifier configuration as shown in Figure 1.



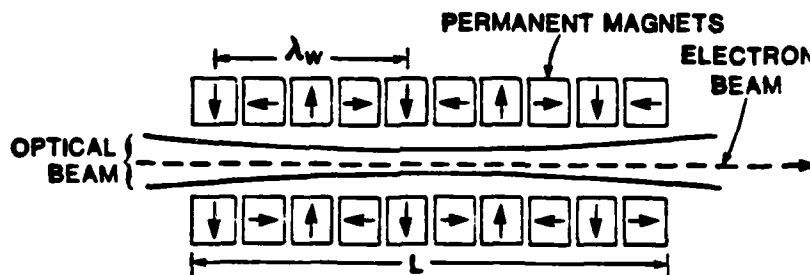
82 06270

Figure 1. Block diagram of apparatus for single-pass electron energy spectrum measurement.

Primary system elements are the RF linac operating at 20 MeV, a two meter wiggler magnet, a gigawatt pulsed CO<sub>2</sub> laser, and an electron spectrograph. The peak e-beam power<sup>2</sup> is substantially lower than the peak photon power, with the result that photon gain is quite small and its unambiguous measurement is difficult.<sup>3</sup> In contrast, the electron energy spectrum clearly shows the large deceleration associated with the tapered wiggler, which in this case has a 9 percent resonant energy change. The hardware is described in the next section, followed by a discussion of the electron spectrograph data. These spectra show a net deceleration of 2.5 percent, with a peak value of about 9 percent.

II. HARDWARE  
 A. Wiggler Magnet

The permanent magnet wiggler has  $\text{SmCo}_5$  bars arranged as shown in Figure 2.



82 06271

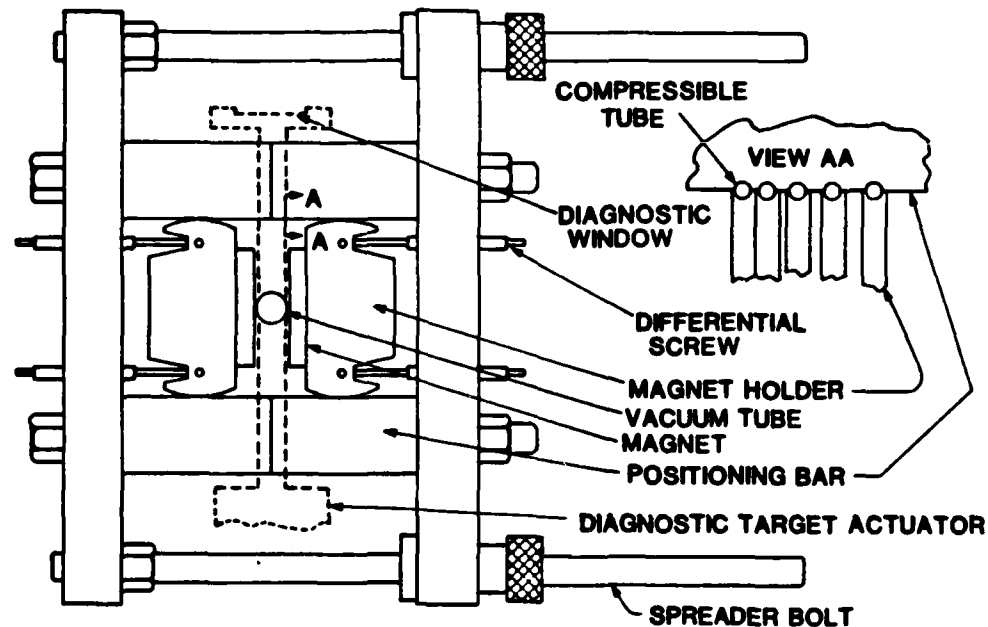
Figure 2. Planar wiggler geometry. Bold arrows on the  $\text{SmCo}_5$  permanent magnets indicate the direction of magnetization. The wiggler actually has  $96 \frac{3}{4}$  wavelengths,  $\lambda_w$ , within the total length,  $L$ .

This scheme, first suggested by Halbach,<sup>4</sup> makes efficient use of the magnetic material and produces a plane polarized field.<sup>5</sup> Parameters such as the gap and magnetic field wavelength are optimized<sup>5</sup> to minimize the photon power required to achieve a given deceleration. The photon beam is focused in the center of the wiggler with a design Rayleigh range of 65 cm and is clipped at the entrance and exit at  $e^{-8}$  of the centerline intensity. This results in an on-axis intensity modulation of about  $\pm 4$  percent.<sup>6</sup> Basic parameters of the wiggler are given in Table 1. Slow variation of the resonant energy along the wiggler length is achieved by change of wavelength at constant gap, with the resonant energy decreasing by 9 percent from entrance to exit. The tapering is chosen so that the stable phase angle<sup>7</sup> is independent of axial position. For this taper the calculated onset of trapping begins at approximately 100 MW photon power.

Table 1  
 WIGGLER PARAMETERS

Total Length	231 cm
Full Gap (magnetic)	1.27 cm
Peak Entrance Field	2.64 kG
Peak Exit Field	2.44 kG
Entrance Wavelength	2.54 cm
Exit Wavelength	2.22 cm
Remanent Field	8800 G
Magnet Dimensions	$0.56 \times 0.83 \times 5.0 \text{ cm}^3$

Aspects of the mechanical design are depicted in the end-view diagram of Figure 3.



82 06272

Figure 3. End view diagram of clamshell wiggler sections enclosing the vacuum tube. Dotted lines indicate the three fluorescent screen diagnostic ports within the wiggler.

Each magnet is cemented to a separate aluminum holder which is, in turn, positioned axially by slots in the positioning bars. The wiggler taper is determined by the location of these slots and can be changed by replacement of the positioning bars. Differential screws provide adjustment of the distance between the center line and each magnet for field tuning purposes and, in addition, allow magnet rotation in the plane of the figure. Such canting is useful for control of e-beam focal properties. For example, with increasing cant angle, the focal strength in the horizontal plane (as drawn) becomes weaker while the vertical plane begins to focus.

A 1/2-in. OD, 0.010-in. wall, Type 310 stainless steel vacuum tube is located between the two halves of the magnet assembly. The tube has five diagnostic ports, one each at the front and rear of the wiggler, and three along its length. Fluorescent screens can be inserted remotely at each port for determination of photon and electron beam positions and profiles. In practice, the beam from a helium-neon laser is made to run along the same line as the CO<sub>2</sub> laser, and the e-beam is positioned on the helium-neon laser spots.

Before assembly, a Hall probe was used to measure the B-field of individual magnets. The probe was placed at locations corresponding to the wiggler center line, and significant variations from magnet-to-magnet

in field strength and uniformity were found. As an example, the distribution of several measured parameters is briefly reviewed. These parameters deal with 1) the average strength of magnetization, 2) the variation in field strength from the north to south pole face, and 3) the misalignment of the polarization vector with respect to the pole face. A pictorial description of the measurement method is shown in Figures 4 and 5. Figure 4 deals with magnets whose magnetization vectors are perpendicular to the electron beam line (Type I) and Figure 5 is for magnets with vectors parallel to the beam line (Type II). These measurements can be summarized roughly as follows: the average field strength varies about  $\pm 1$  percent. The gradient from the north to south faces of Type I magnets is about  $\pm 2$  percent. Modeling of the rotation parameter for Type II magnets shows that the polarization vector is misaligned with respect to the magnet body by roughly  $\pm 1$  degree. This rotation is about an axis that is perpendicular to the B-field plane of the wiggler (the plane of the page in Figure 2). Rotation about the other axis was not measured prior to assembly.

Simulations of the FEL including the imperfect magnets show no significant loss of interaction strength due to phase and amplitude noise in the ponderomotive potential. However, field imperfections such as these can cause significant steering errors and terminate the interaction by loss of electron-photon overlap. A magnet grouping algorithm has been devised for the selection and ordering of magnets in the wiggler so as to compensate for steering errors in the wiggle plane and to maintain mid-plane symmetry. The algorithm is based on a calculation of the anomalous steering in the wiggler plane caused by the nonideal field components of individual magnets.

When assembled, additional Hall probe measurements show that the wiggler field has a 1 percent RMS variation in field measured at maximum field points, and a 1 percent RMS deviation in the distance between successive zero crossings. These measurements were not sufficiently accurate to provide reliable steering error information, but steering in the wiggle plane was measured by means of a floating wire technique. A several milliradian error was found near the wiggler entrance. It was initially corrected by moving several magnets slightly, and later the magnets were returned to their nominal positions and external Helmholtz trim coils were used for correction. Floating wire measurements with the trim coils in place indicate a maximum electron deviation of 0.2 mm in this plane.

In the plane of the B-field, a combination of floating wire and Hall probe techniques were used to assess steering. Application of the floating wire in this plane presents difficulty because the wire tends to avoid the centerline, but a suitable technique for quantitative measurement of the steering was devised. It is described elsewhere.<sup>8</sup> An example of the Hall probe measurement of the error field perpendicular to the B-field plane (nominally field free) is given in Figure 6.

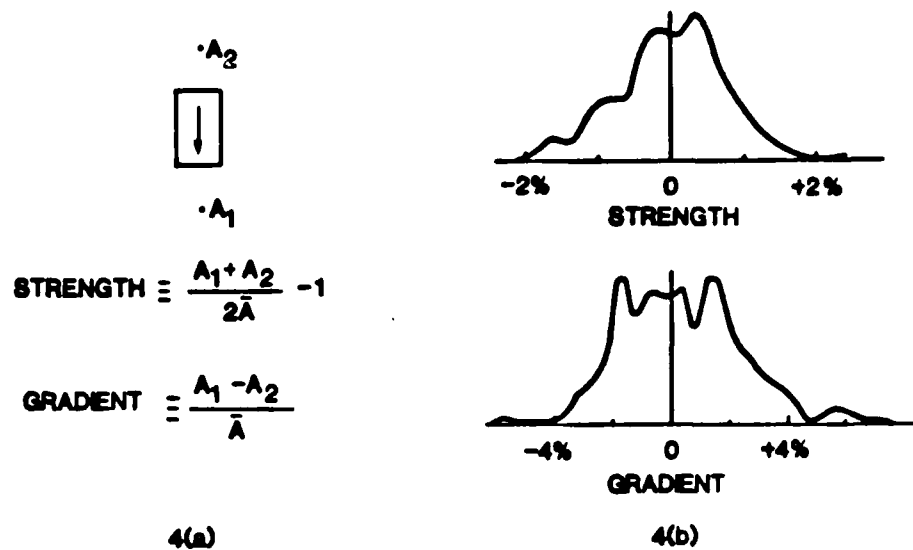


Figure 4. Type I magnet strength and gradient distributions. a)  $A_1$  and  $A_2$  are locations for Hall probe measurements on magnets with magnetization vectors perpendicular to e-beam (Type I). The probe is oriented to measure the vertical component of the field. The strength and gradient parameters are determined for each magnet as indicated.  $\bar{A}$  is the average value for all measurements of all Type I magnets. b) Probability distribution of strength and gradient parameters for 500 Type I magnets.

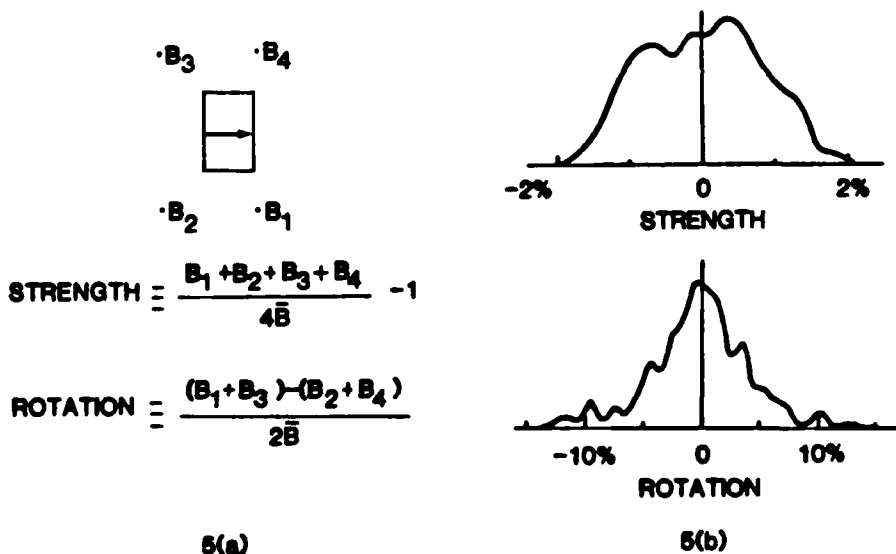
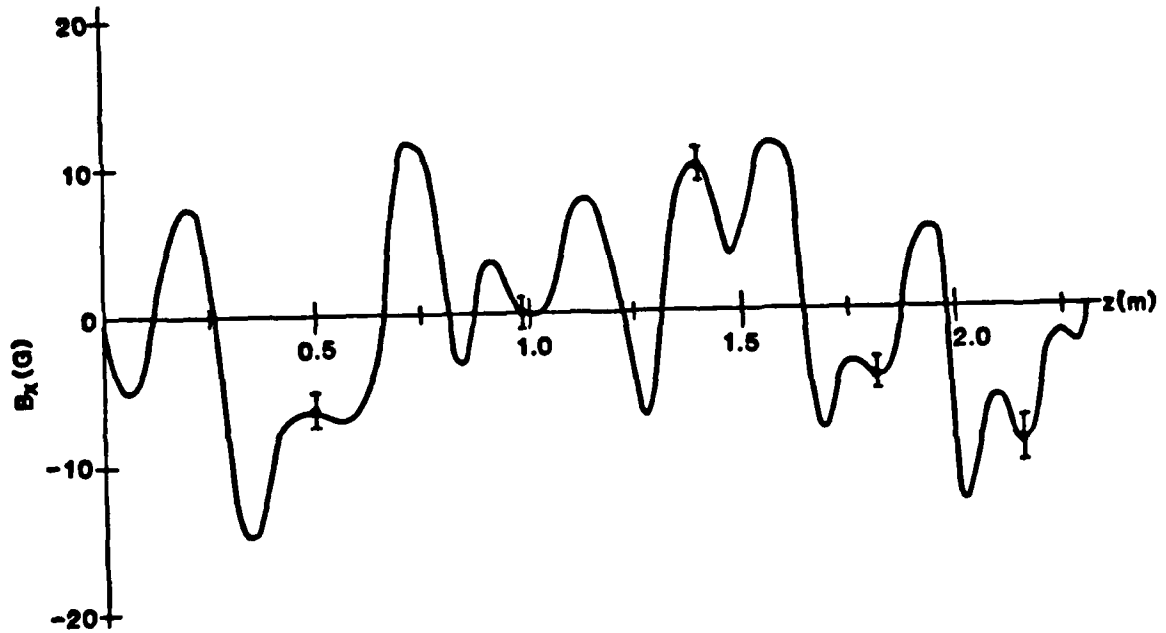


Figure 5. Type II magnet strength and rotation distributions,  $B_1$ ,  $B_2$ ,  $B_3$ , and  $B_4$  are locations for Hall probe measurements on magnets with magnetization vectors parallel to the e-beam (Type II). The probe is oriented to measure the vertical component of the field. The strength and rotation parameters are determined for each magnet as indicated.  $\bar{B}$  is the average value for all measurements of all Type II magnets. b) Probability distribution for strength and rotation parameters for 500 Type II magnets.



02 05917

Figure 6. Measured error field of assembled wiggler with Hall probe oriented to measure field perpendicular to nominal B-field plane. The wiggler entrance is at  $z = 0$  and exit is at  $z = 2.3$  m. The data has been smoothed by averaging over several wiggler wavelengths.

In this figure, a small oscillating component of the main wiggler field has been removed by averaging the data over several wiggler wavelengths. The oscillating component was of comparable magnitude to the error field. The error field shown apparently results from misalignment of magnetization vectors with respect to the magnet bodies, although the degree of misalignment was not measured for individual magnets. Modeling indicates that a 1 degree random orientation error would account for errors of this size. Recent measurement of field misalignment for individual magnets which were not used in the wiggler, but manufactured in the same batch as those that were, show that errors up to  $\pm 2$  degrees are typical. This refers to misalignment in the direction which produces field components perpendicular to the B-field plane.

The steering error calculated from Figure 6 acts synergistically with the focusing that results from the normal B-field transverse gradients. Errors near the wiggler entrance excite a Betatron oscillation and the oscillation is reinforced by the errors in the middle portion of the wiggler. A calculated trajectory including the steering errors and focusing is shown in Figure 7.

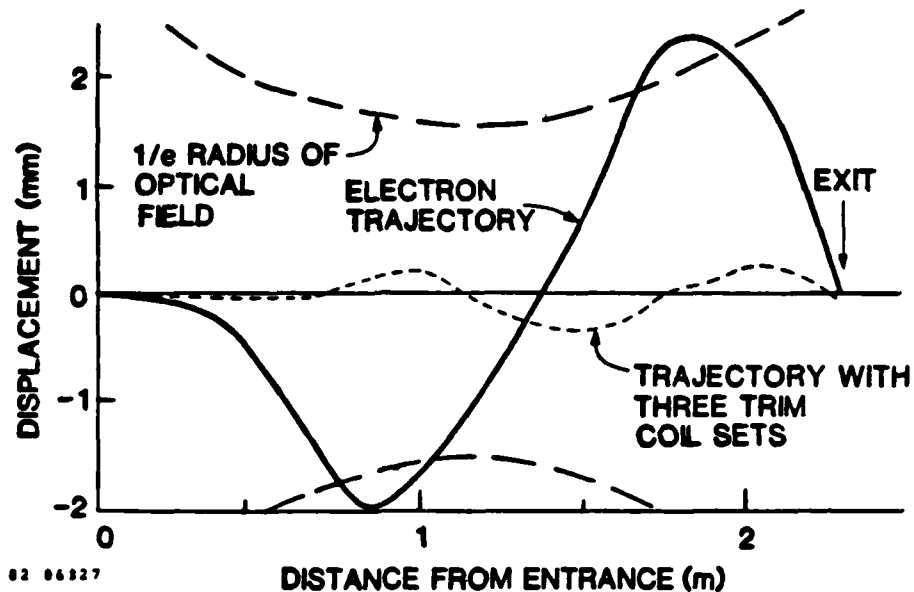


Figure 7. Calculated trajectories in nominal B-field plane. The calculation is based on the field measurements of Figure 6 and the calculated focal properties in this plane.

It is calculated on the assumption that the electron enters the wiggler along the centerline, and shows that the calculated trajectory exceeds the  $1/e$  point in the photon beam at two locations. The calculated trajectory with correction coils in place is also shown. The expected trajectory deviation in this plane is less than 0.3 mm.

#### B. RF Linac and E-Beam Line

The Boeing Linac is a traveling-wave radio-frequency linear accelerator capable of acceleration to 30 MeV. The primary power is supplied by a single 20 MW peak, 2 kW average, S-band klystron. A gridded gun provides macropulse widths over the range of 0.005 to 10  $\mu$ sec. Two stages of bunching at the fundamental frequency compress the charge into 15 to 20 degrees of phase of the accelerating wave to achieve an energy spread of less than 2 percent. The output pulse train consists of approximately 20 psec pulses separated by the 350 psec RF cycle time. Peak micropulse currents are from 2 to 5 amps, and values detected at the spectrograph were somewhat lower due to transmission losses. The normalized beam emittance,  $\epsilon$ , defined as  $\gamma\pi\alpha'$ , is approximately 0.015 cm radians in each plane, without emittance filtering. The typical energy spread (full width, half maximum) in the e-beam at the wiggler is  $\Delta\gamma/\gamma < 0.02$ .

The e-beam transport and optics system is shown in Figure 8.

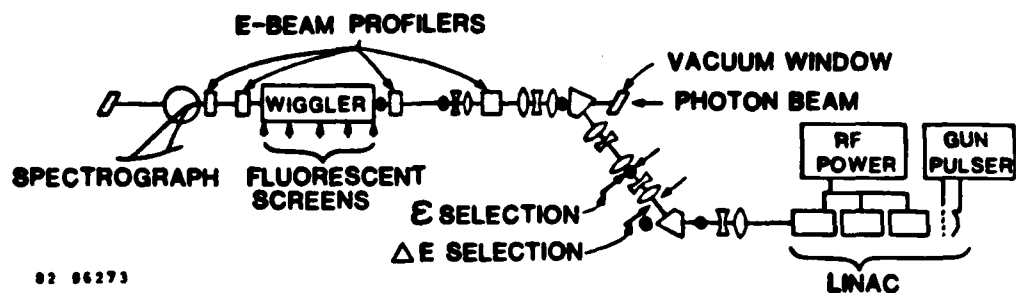


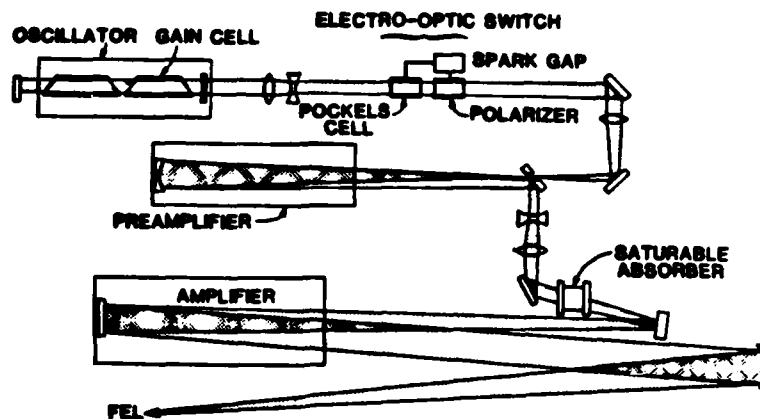
Figure 8. Schematic diagram of electron beam line. Magnetic lenses are focusing and defocusing as shown for motion in the plane of the page. The location of profile and position monitors are indicated by dots. Five additional monitors, marked by arrows, are in the wiggler.

The system provides acromatic transport to the FEL with adjustable energy and emittance filtering. The beam is switched into the FEL experiment line by a dog-leg translation system similar to a design suggested by Swenson. A feature of the translation system is that energy and emittance encoding occur at convenient positions outside the magnetic elements. Mechanical slits at these locations provide for energy and emittance selection. Five quadrupoles are used to shape the input beam. Wirescan profile monitors upstream and downstream of the wiggler, together with the fluorescent screens in the wiggler, are used to measure the input parameters, namely the beam position, size, and convergence angle in each plane. In practice, it has proved difficult to achieve the proper beam envelope along the full length of the wiggler. To study this problem, a new set of beam profile and position monitors has been added at locations indicated by dots in Figure 8. These new screens will facilitate placement of the e-beam on the centerline of the magnetic optics, and thereby serve to reduce beam aberration caused by off-axis use of the optics. Unnecessary aberration may exacerbate the problem of improper beam size in the wiggler.

The electron spectrograph is a 12-inch round pole Browne Beuchner<sup>10</sup> design, with a design energy range of 16 to 22 MeV. The focal plane has been segmented into 20 stopping-block channels with each channel cabled to an independent oscilloscope channel. The spectral bandwidth of the detection system is approximately 200 MHz. Principal limits to spectrograph resolution are the magnification due to beam size and beam divergence angle. Calculated energy uncertainty due to a worst case estimate of 1 cm diameter beam size or 3 mrad divergence immediately upstream of the roundpole magnet is equivalent to  $\Delta\gamma/\gamma = 0.002$ . The resolution is further limited by the finite size of the stopping blocks to no better than 0.5 percent. The energy calibration and position-angle sensitivity have been established experimentally with floating wire techniques. Agreement between the design and measured dispersion is within 0.5 percent, and sensitivity to the nonideal effects of beam size and angular content are consistent with calculations.

### C. CO<sub>2</sub> Laser

A block diagram of the CO<sub>2</sub> laser system is shown in Figure 9.



02 00176

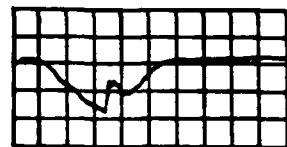
Figure 9. CO<sub>2</sub> laser oscillator-amplifier configuration.

Major elements of the system are the single mode oscillator, followed by a double pass preamp and double pass amplifier. The electro-optic switch between the oscillator and preamp serves to limit pulse length and thereby reduce energy loading on the NaCl windows (not shown) which isolate the vacuum system. A low pressure discharge in the gain cell enables the oscillator to operate on a single longitudinal mode of the optical cavity. Limitation to one transverse mode is made by aperturing the oscillator cavity, with apertures at all other points in the system being sufficiently large to avoid significant clipping. The saturable absorber cell is necessary to eliminate self oscillation of the preamplifier and amplifier when metal surfaces of the e-beam vacuum system act as mirrors.

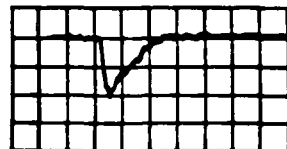
The system produces gain-saturated 20 J pulses of 40 nsec length with a peak power of 1.5 GW occurring near the leading edge. The output beam is approximately diffraction limited as verified by measurement of the beam profile through the waist region with a pyroelectric detector array. These measurements are not sufficiently detailed to yield a Strehl ratio. The CO<sub>2</sub> beam is aligned with the mechanical axis of the wiggler by direct referencing of the CO<sub>2</sub> spot to the entrance and exit of the wiggler.

### III. ELECTRON ENERGY SPECTRUM MEASUREMENTS

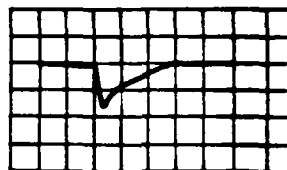
Electron energy gain or loss resulting from the FEL interaction is measured with the electron spectrograph. In these experiments, the interaction is easily identified in the time-resolved spectra since the optical pulse has different temporal behavior than the electron macropulse. While the temporal resolution is sufficient to resolve the FEL interaction on the macropulse, the individual micropulses are unresolved. Representative current histories can be seen in Figures 10a and 10b, where traces from two of the twenty spectrograph channels are shown for the same shot.



A



B



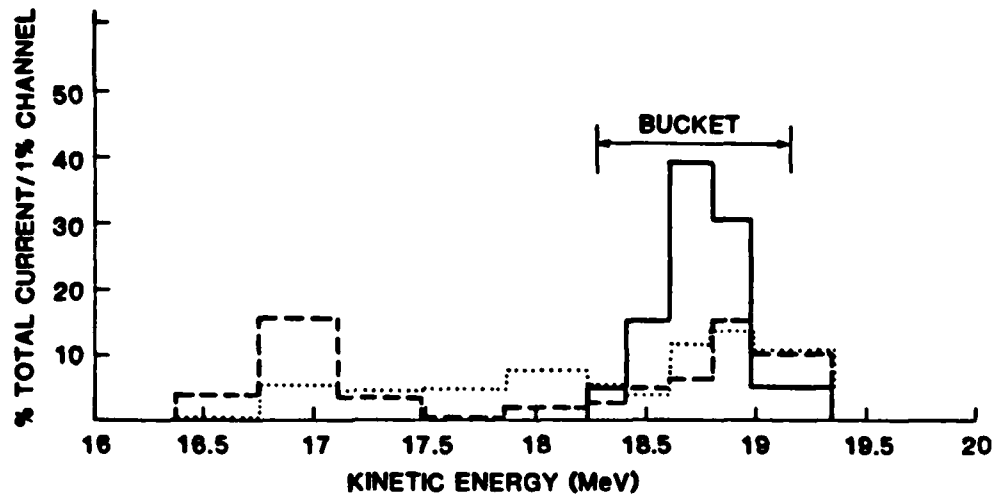
C

Figure 10. Time histories of spectrograph current and CO<sub>2</sub> laser power. Trace A is current on a spectrograph channel located within the energy width of input e-beam. Reduction of signal near the center of the macropulse is due to the FEL interaction. Trace B is the same except that this channel is at lower energy than the input pulse, and the oscilloscope sensitivity is greater. Trace C is the photon pulse. The abscissa is 20 ns/div for all.

02 06:75

The zero current baseline, the macropulse, and the short interaction spike corresponding to the presence of the photons, are all seen clearly in trace a. In this case, the interaction momentarily reduces the current by about one half and, of course, the difference must appear in other channels. Trace b is for a channel at energy less than the initial beam energy, and hence does not show the macropulse envelope, but only current resulting from the interaction. This channel shows zero current in the absence of the CO<sub>2</sub> laser beam. The optical pulse, as seen by a pyroelectric detector viewing a portion of the beam reflected from the NaCl vacuum entrance window, is shown in Figure 10c with 100 MHz bandwidth. Note that the current pulse shape seen on any spectrograph channel is not expected to closely match the optical pulse shape because of nonlinear effects germane to the tapered-wiggler FEL.

Electron energy spectra with and without the CO<sub>2</sub> laser beams are shown in Figure 11.



02 06276

Figure 11. Electron energy spectra. The dotted and solid lines are measured spectra for a given macropulse, with and without photons, respectively. The dashed curve is a calculated output spectrum based on the solid line input spectrum, 800 MW CO<sub>2</sub> laser power, and ideal electron-photon overlap. The full width and location of the calculated ponderomotive potential well at the wiggler entrance is indicated.

The solid line shows the spectrum measured several nanoseconds prior to the laser pulse, and the dotted line shows the spectrum measured at the time of peak CO<sub>2</sub> intensity. The curves can be considered as input and output spectra, respectively, since the macropulse current and spectral content do not change significantly on several nanosecond timescales. The photon pulse, not shown, has a peak power of approximately 800 MW. In this case, the spectrograph channels are connected in pairs externally to an effective width of 1 percent from 18.2 to 19.0 MeV and a 2 percent effective width elsewhere. For any channel, the uncertainty in current at the time of maximum photon flux is not more than 25 percent. Another indication of the degree of reliability is that the total current in the interaction and non-interaction traces typically differs by less than 10 percent. The total current at the time of the interaction is about 50 ma.

The shift of energy centroid from the input to the output spectra is 2.5 percent, assuming the current to be evenly distributed within each spectrograph channel. This 2.5 percent net extraction is the highest achieved to date in this experiment, but it is lower than expected. Using the input spectra of Figure 11, an electron energy spectrum including the interaction has been calculated by direct integration of the equations of motion for energy loss and electron phase in the ponderomotive potential. In the calculation it is assumed that the e-beam is much smaller than the photon beam and is located precisely on the photon beam axis. The result is the dashed line curve of Figure 11, which yields a net extraction of 4.1 percent. The difference in peak deceleration for the two spectra is small and could be the result of an energy offset between the actual and assumed entrance resonant energy. The curves differ most significantly at the intermediate energies around 18 MeV, where substantial current is found in the measurement but not the calculation. This difference is the result of electron detrapping from the ponderomotive potential well in the central portion of the wiggler, and it stems from an oversize e-beam. Observation of the e-beam fluorescent spots within the wiggler shows a proper alignment, but on most screens the e-beam is larger than the  $1/e$  radius of the photon electric field. Degradation of electron extraction then occurs due to both the effective loss of E-field, and also to an apparent increase in electron energy spread caused by the B-field gradient. Both problems are expected to be unimportant in this experiment when the e-beam is within the  $1/e$  envelope of the E-field. As mentioned in Section IIB, the reason for the large beam size in the wiggler is not well understood and is currently being investigated. A quantitative assessment has not yet been made to determine whether the measured spectrum is consistent with the observed beam envelope.

#### IV. SUMMARY

An experiment for verification of basic aspects of the tapered-wiggler FEL has been described. In particular, the electron energy distribution resulting from the interaction has been examined in a single pass configuration with the necessary large photon power supplied by an external  $\text{CO}_2$  laser. Deceleration of individual electrons by an amount approximately equal to the energy taper of the wiggler magnet is observed. A net deceleration of 2.5 percent has been achieved, compared to a predicted value of 4 percent. The discrepancy is a result of electron detrapping along the wiggler length and results from an oversize electron beam.

#### ACKNOWLEDGEMENTS

The authors wish to acknowledge the assistance of R.W. Nelson and J.M. Ross of Mathematical Sciences Northwest, Inc., and R.C. Kennedy, L. Tyson and A.D. Yeremian of Boeing Aerospace Company. In addition, the generous support of the overall program by D.R. Shoffstall of Boeing is appreciated.

#### REFERENCES

1. N.M. Kroll, P.L. Morton, and N.M. Rosenbluth, "Variable Parameter Free-Electron Laser," in Free-Electron Generators of Coherent Radiation, Phys. of Quantum Electronics, Volume 7, S.F. Jacobs, Editor, Addison-Wesley Publishing Company, 1980, p. 113.
2. D.A.G. Deacon, L.R. Elias, J.M.J. Madey, G.J. Ramian, H.A. Schwettman, and T.I. Smith, "First Operation of a Free-Electron Laser," Phys. Rev. Lett. 38: 892 (1977).
3. It is difficult to separate the effect of gain and phaseshift when the interaction is weak, because some signal enhancement techniques do not discriminate between gain and phaseshift. A discussion of gain measurement techniques for conditions similar to those of this experiment is found in B.E. Newnam, K.L. Hohla, R.W. Warren, and J.C. Goldstein, "Optical Diagnostics for the Los Alamos Free-Electron Laser Amplifier Experiment," IEEE J. Quant. Elect. QE-17: 1480 (1981).
4. K. Halbach, "Physical and Optical Properties of Rare Earth Cobalt Magnets," Presented at International Conference on Charged Particle Optics, Giessen, West Germany, 8-12 September 1980.
5. J.M. Slater, "Tapered-Wiggler Free-Electron Laser Optimization," IEEE J. Quant. Elect. QE-17: 1476 (1981).
6. A.J. Campillo, J.E. Pearson, S.L. Shapiro, and N.J. Terrell, "Fresnel Diffraction Effects in the Design of High-Power Laser Systems," Appl. Phys. Lett. 23: 85 (1973).
7. J. Lobb, L'onde Electrique 27: 27 (1947).
8. D.C. Quimby, "Floating Wire Measurement of Transverse Magnetic Field Errors in a Planar Free-Electron Laser Wiggler," to be published in J. Appl. Phys.
9. D.A. Swensen, "Acromatic Translation System for Charged-Particle Beams," Rev. Sci. Instr. 35: 608 (1964).
10. C.P. Browne and W.W. Beuchner, "Broad Range Magnetic Spectrograph," Rev. Sci. Instr. 27: 899 (1956).

## Appendix B

### Calculations of FEL Performance Including Finite Emittance

The FEL interaction is often modeled by assuming that all electrons travel straight down the magnetic axis of the device and are ideally aligned with the photon beam. Unfortunately, this ideal situation is not achieved in practice due to finite e-beam emittance and improper beam preparation and alignment. An FEL interaction model has been developed to calculate the sensitivity of the MSNW extraction experiment to these factors.

### Electron Tracking Equations Including Finite Emittance

The usual electron tracking equations for a single on-axis electron are

$$\begin{aligned} \text{(a)} \quad \frac{dy}{dz} &= \frac{-e a_s \sin\psi}{\gamma} & [1] \\ \text{(b)} \quad \frac{d\psi}{dz} &= k_w - \frac{k_s}{2\gamma^2} \left[ 1 + a_w^2 \right], \end{aligned}$$

where the parameters  $e_s$ ,  $a_w$ , and  $k_w$  are functions of  $z$  only and  $k_s$  is a constant. The resonance condition is given by  $d\psi/dz = 0$ , which leads to an expression for the resonant energy

$$\gamma_r^2 = \frac{\lambda_w}{2\lambda_s} \left[ 1 + a_w^2 \right]. \quad [2]$$

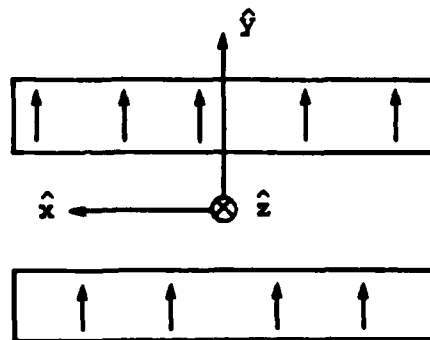
The FEL interaction is typically modeled by numerical integration of the tracking Eqs. [1a and b] which describe the motion of individual electrons in  $\gamma$ - $\psi$  space. For a monoenergetic beam, tracking of 20-30 electrons initially evenly distributed from  $\psi = -\pi$  to  $\pi$  is sufficient to model an amplifier extraction experiment. Inclusion of initial energy spread is

straightforward; several groups of 20-30 electrons with different initial  $\gamma$ 's is all that is required. In reality, however, the e-beam has finite emittance, and many electrons are injected off axis. They follow sinusoidal betatron orbits in the focusing plane and (for a planar wiggler) straight-line ballistic trajectories, with a finite angle relative to the axis, in the wiggle plane (neglecting the small individual wiggles). These off-axis trajectories reduce the spatial overlap with the photon beam, in addition to detuning the FEL interaction by inducing an apparent energy spread.

When off-axis electron trajectories are included, the tracking equations must be modified to include gradients in the magnetic field and photon intensity, as well as detuning due to finite transverse velocities. For a planar wiggler with the coordinate convention defined in Fig. 1, the tracking equations become

$$\frac{d\gamma}{dz} = \frac{-e_s a_w \sin\psi}{\gamma} \quad [3]$$

$$\frac{d\psi}{dz} = k_w - \frac{k_s}{2\gamma^2} \left[ 1 + a_w^2 + \gamma^2 (\theta_x^2 + \theta_y^2) \right].$$



82 86775

Figure 1. Coordinate Convention for Planar Wiggler.

The spatial distribution of the electric field of an axisymmetric Gaussian optical beam is

$$e_s(x, y, z) = e_s^0 \left( \frac{w_0}{w} \right) \exp[-(x^2 + y^2)/w^2] \quad [4]$$

$$w(z) = w_0 \left[ 1 + \frac{(z - z_w)^2}{Z_r^2} \right]^{1/2}$$

where,  $Z_r = \pi w_0^2 / \lambda$  is the Rayleigh range

$e_s^0$  = the peak e-field at the waist

$z_w$  = the axial position of the waist,

the normalized B $\lambda$  product is

$$a_w(y, z) = a_w(z) \cosh k_w y, \quad [5]$$

and, as usual,

$$k_w = k_w(z) \quad [6]$$

and  $k_s = \text{constant}$ .

The angles of the electron trajectory relative to the axis

$$\theta_x = \frac{dx}{dz} \quad [7]$$

$$\theta_y = \frac{dy}{dz}$$

now appear in the equations in such a way as to change the resonant energy to

$$\gamma_r^2 = \frac{1 + a_w^2}{\frac{2\lambda_s}{\lambda_w} - \theta_x^2 - \theta_y^2} \quad [8]$$

Of course, off-axis excursions in the focusing plane also lead to changes in the resonant energy through the  $y$ -dependence of  $a_w$  (Eq. [5]).

Two new versions of the MSNW tracking code have been developed to integrate the revised tracking Eq. [3]. The two versions, named BETATRAK and WIGLTRAK, allow finite e-beam emittance in the focusing plane and wiggler plane, respectively. Presently, non-zero initial displacement and/or angle is allowed in only one phase plane at a time. The codes compute trajectories based on the initial  $\gamma$  for each of several phase space groups with different entrance displacements and angle. Each of the 20-30 electrons tracked in each phase space group is assumed to follow this trajectory regardless of whether it is actually trapped and decelerated; this assumption is quite adequate for the moderate wiggler tapers of interest.

#### Maximum Emittance Acceptance

These models have been used to calculate the emittance acceptance of the MSNW amplifier experiment. The calculations used the actual wiggler taper (designed to have constant phase angle  $\psi$  for a resonant electron) and assumed an ideal Gaussian photon beam with Rayleigh range of 65 cm centered on the axis. For simplicity, a monoenergetic beam with the entrance resonant  $\gamma$  was used.

Figure 2 presents the phase space acceptance envelope within which the extraction exceeds 50 percent of the value for electrons injected exactly collinear with the axis. This envelope is quite symmetric

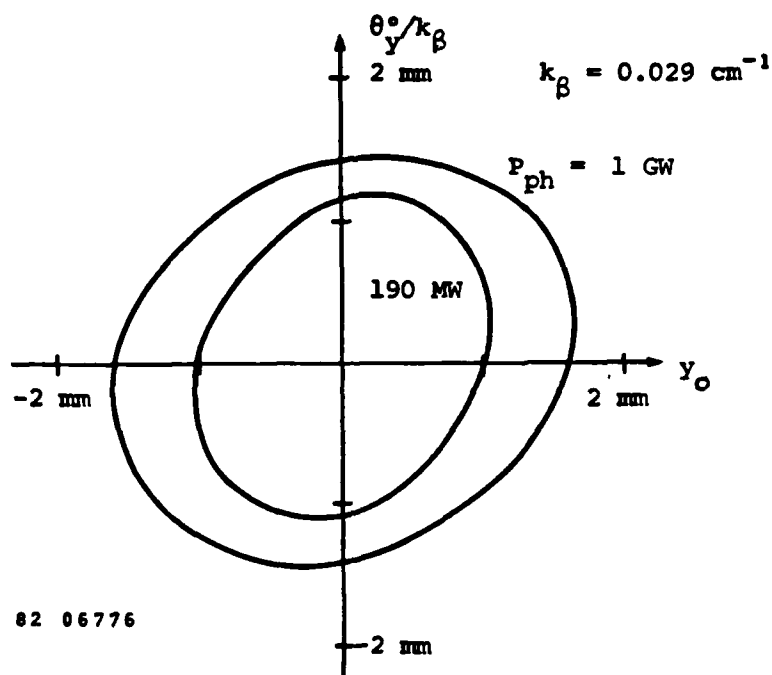


Figure 2. Phase Space Acceptance Envelope in Focusing Plane. Contours show where extraction drops to 50 percent if its on-axis value.  $\gamma_0 = 37.91$ ,  $Z_R = 65 \text{ cm}$ ,  $x_0 = 0$ ,  $\theta_0^0 = 0$ .

in phase space when the angle is normalized by  $k_\beta = 0.029 \text{ cm}^{-1}$ , the betatron wavenumber. This is a convenient normalization, since a betatron orbit with maximum displacement  $y_0$  has a maximum crossing angle  $\theta = y_0 k_\beta$ . The monoenergetic e-beam is assumed to enter with the energy which is resonant for electrons injected collinear with the axis (Eq. [2]). This energy is by no means optimal, since all electrons injected with finite displacement or angle in the focusing plane are then detuned by the amount which can be calculated from [8]. Within the phase space envelopes, the extraction is fairly uniform as shown in Fig. 3. Beyond the 50 percent point, the extraction plummets precipitously. In this figure, detuning in position is shown to be nearly equivalent to detuning by angle if  $\theta = k_\beta y$ . They would be exactly equivalent except that the overlap with the photon beam differs in the two cases. In the focusing plane, however, loss of overlap is a very small effect compared to the detuning in energy. Increasing the intensity of the optical beam increases the size

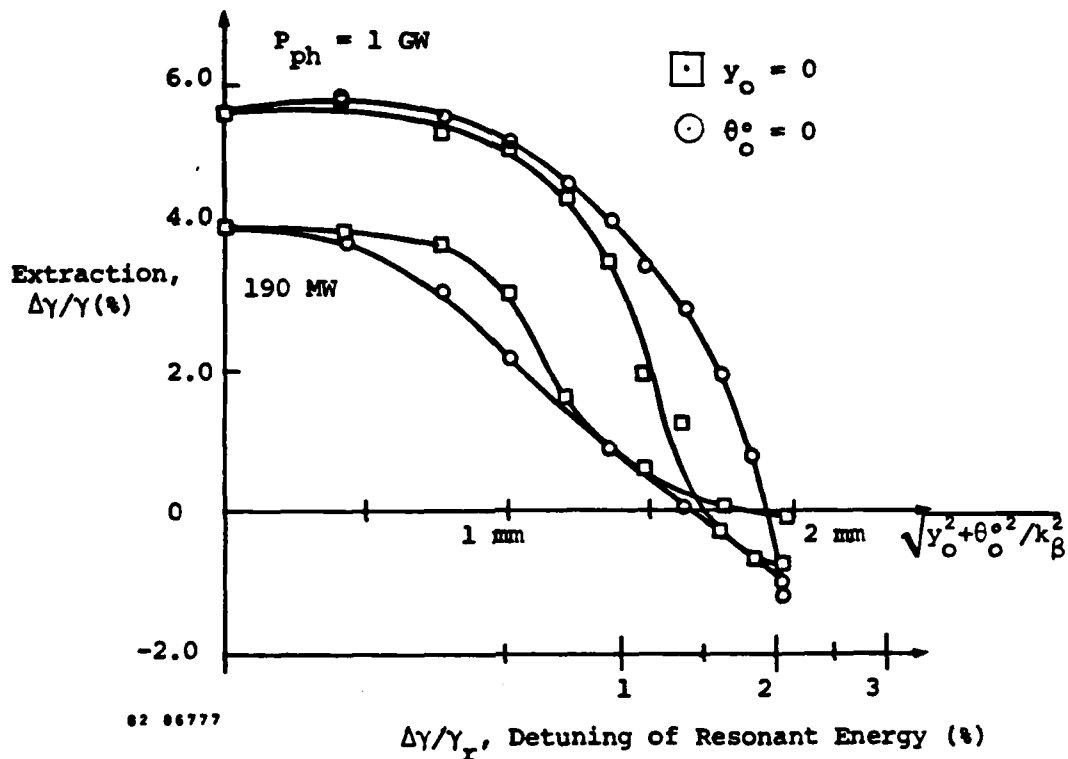


Figure 3. Extraction as a Function of Distance Off-Axis in Focusing Plane Phase Space.

of the acceptance envelope, as shown in Fig. 2. This comes about because the bucket depth increases, allowing net extraction at greater detuning. The peak extraction increases as well, as shown in Fig. 3. The phase space acceptance envelope for the wiggler plane is depicted in Fig. 4. In this case there is no focusing so that loss of overlap with the laser beam is far more critical than detuning. In contrast to the results in the focusing plane, were it is desirable to have a focused e-beam at the entrance, the e-beam and photon beam waists should be coincident in the wiggler plane. As shown in Fig. 5, the curves of extraction versus phase space location have a qualitatively different shape in the wiggler plane. As the displacement in phase space increases, the extraction does not suddenly drop to zero, but rather decreases to less than one-half its peak value and then decays more gradually beyond that point. This result is due to detrapping occurring near the photon waist, at one-half the wiggler length. In the focusing plane phase space, as the emittance is increased,

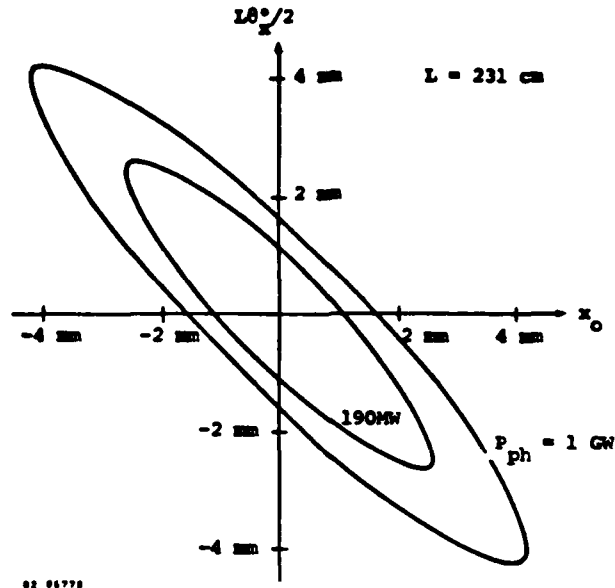


Figure 4. Phase Space Acceptance Envelope in Wiggler Plane. Contours show where extraction drops to 50 percent of its on-axis value.  $\gamma_0 = 37.91$ ,  $Z_R = 65$  cm,  $y_0 = 0$ ,  $\theta_y = 0$ .

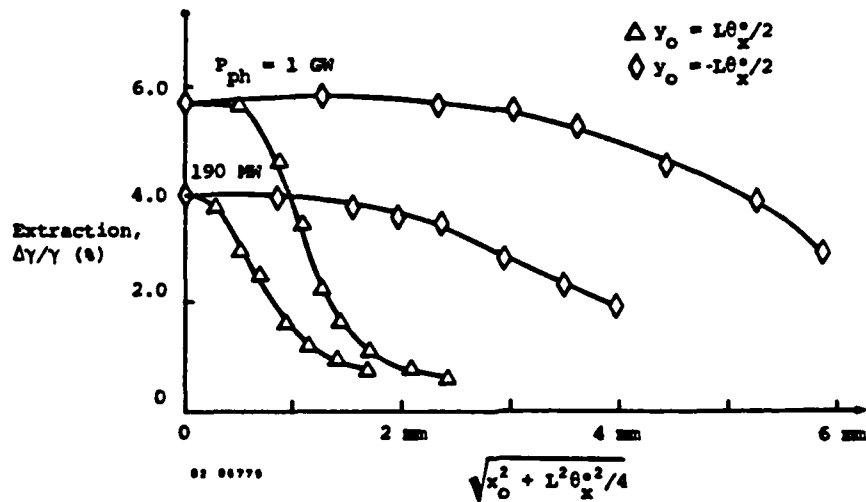


Figure 5. Extraction as a Function of Distance Off-Axis in Wiggler Plane Phase Space.

there essentially is a threshold beyond which there is no trapping. In contrast, there is at least partial trapping in the wiggle plane until the electrons reach the optical beam waist, beyond which they either are or are not trapped depending on the overlap at the waist. This type of effect is clearly seen when the output electron spectra is examined. Tapered wigglers produce a double humped energy spectrum due to the trapping phenomenon. Large emittance in the focusing plane reduces the amount of trapping which initially occurs thereby reducing the size of the low energy hump in the spectrum while retaining the double humped structure. In contrast, large emittance in the wiggle plane causes detrapping midway down the wiggler. This results in "filling in" between the 2 humps, and consequent loss of the double humped structure of the spectrum. Electron spectra are presented in the following section.

#### **Emittance Acceptance with Non-Optimum Entrance Conditions**

The allowed emittance, based on the envelope drawn at the point of 50 percent loss of extraction, is approximately

$$\epsilon_{\text{allow}} \approx 67 \text{ mm mrad} - \text{focusing plane}$$

$$\epsilon_{\text{allow}} \approx 57 \text{ mm mrad} - \text{wiggle plane}$$

for the photon power of 750 MW nominally used experimentally. These results, of course, are based on treating each plane independently. This represents an upper bound on the emittance acceptance. If emittance in both planes was included simultaneously, the allowed emittance would be somewhat smaller.

It is interesting to examine the effect on the electron spectra when emittance is increased and various types of electron beam misalignment are introduced to the calculations. Comparison of the calculated spectra and observed spectra may provide an indication of the types of problems present in the experiment.

Figure 6 presents calculated electron spectra for values of emittance in the focusing plane less than and greater than the allowed emittance. An energy spread of 2% full width is simulated by injecting half the electrons at an energy 0.5% lower than the resonant energy and half at 0.5% higher energy. The emittance phase space is assumed to be uniformly filled. The space space is divided into a number of equal size bins of area approximately 0.17 mm mrad. Increasing emittance in the focusing plane reduces the net extraction while retaining the double humped electron spectrum. Results are qualitatively similar when various degrees of e-beam misalignment are introduced in the focusing plane.

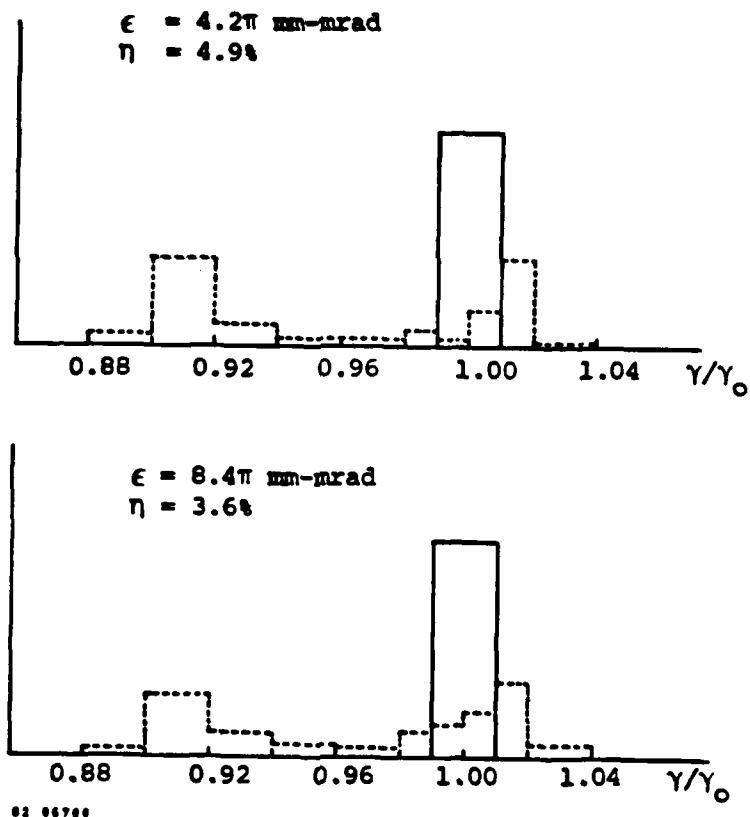


Figure 6. Calculated Electron Spectra for Two Values of Emittance in the Focusing Plane  $\gamma_0 = \gamma_r = 37.91$ . Beam ideally prepared with  $y_{\max} = \theta_{\max}/k\beta$  and no misalignment.  $P_{ph} = 750$  MW,  $Z_R = 65$  cm,  $x_0 = 0$ ,  $\theta_x^0 = 0$ .

Figure 7 shows electron spectra for two values of emittance in the wiggler plane. As the emittance is increased, electrons begin to detrap at intermediate values of deceleration, which tends to fill in the double humped structure. This is particularly evident if the e-beam is improperly prepared or slightly misaligned in this plane. Figure 8 shows two examples, spectra produced when the e-beam is injected 1 mm (1/3 the beam waist diameter) to one side and when the e-beam waist is produced a quarter of the way down the wiggler rather than at L/2.

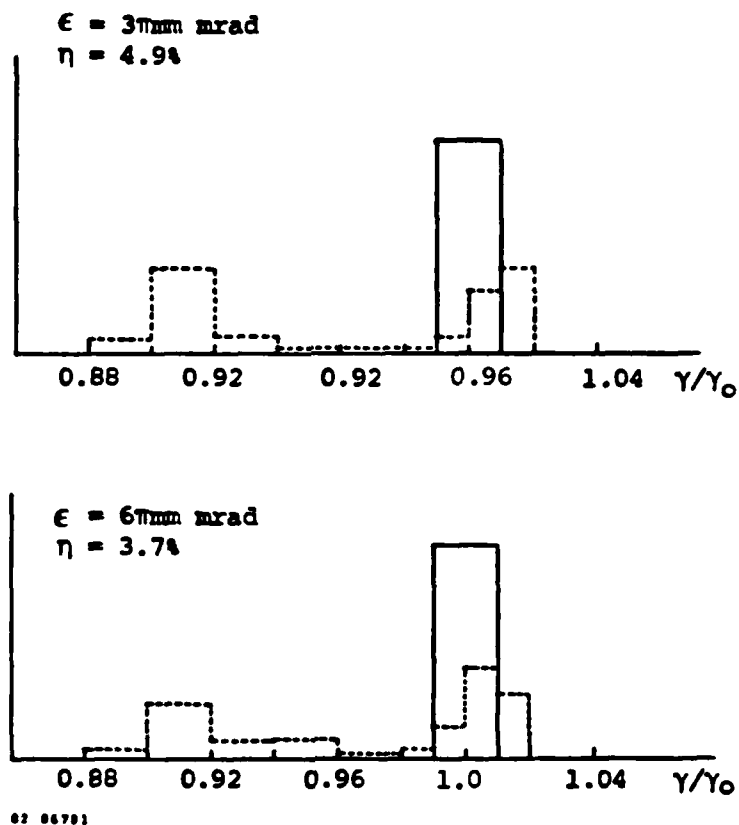
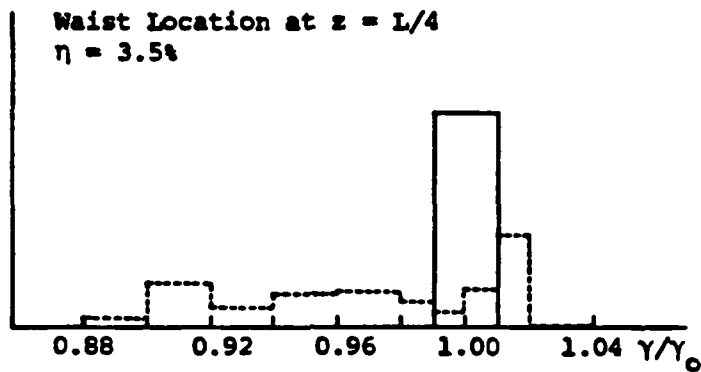
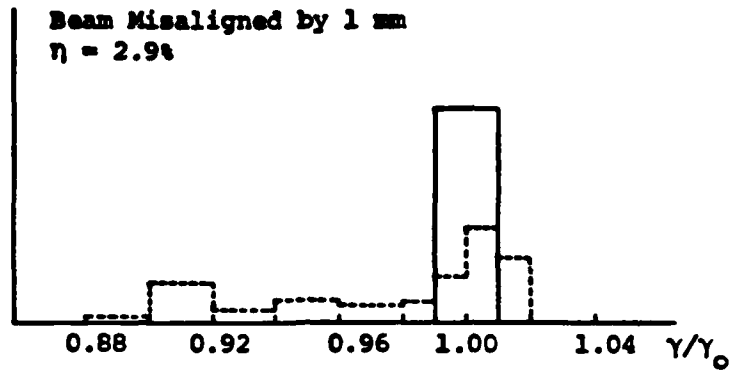


Figure 7. Calculated Electron Spectra for Two Values of Emittance in the Wiggler Plane.  $\gamma_0 = \gamma_r = 37.91$ . Beam ideally prepared with  $x_{\text{max}}/\theta_{x_{\text{max}}} = 33 \text{ cm}$  and no misalignment.  $P_{\text{ph}} = 750 \text{ MW}$ ,  $X_R = 65 \text{ cm}$ .  $y_0 = 0$ ,  $\theta_y^0 = 0$ .



02 00702

Figure 8. Calculated Electron Spectra for Two Types of Beam Misalignment in the Wiggle Plane.  
 $\epsilon = 6\text{mm mrad}$ .  $\gamma_0 = \gamma_x = 37.91$ . Beam otherwise ideally prepared:  $x_{\text{max}}/\theta_{x\text{max}} = 33\text{ cm}$ .  
 $P_{\text{ph}} = 750\text{ MW}$ ,  $Z_R = 65\text{ cm}$ ,  $y_0 = 0$ ,  
 $\theta_x^0 = 0$ .

## APPENDIX C

### Mode Structure of a Tapered-Wiggler Free-Electron Laser Stable Oscillator

#### I. INTRODUCTION

The tapered-wiggler free-electron laser (FEL) is of current interest for its potential as an efficient, tunable laser. The basic idea is a variation of the FEL concept demonstrated in the experiment of Deacon, et al.[1], in which it was shown that a small fraction of electron-beam kinetic energy could be converted to optical energy in a single pass through a wiggler magnet. The tapered-wiggler concept[2] involves variation, or tapering, of the wiggler parameters as a function of axial position in such a manner as to maintain a resonant interaction as the electrons decelerate. This tapering allows increased kinetic energy extraction per pass, and may lead to high efficiency systems through reduction of e-beam recirculation or energy recovery requirements.

Several verification experiments of the basic concept are in progress[3]. Initial experiments are expected to achieve only low photon gain, and in a sense provide validation only of the relatively simple theory describing electron deceleration in predetermined photon and wiggler fields. The process of self-consistently determining electron and photon behavior in high gain amplifiers or oscillators is significantly more complex, and has recently been the subject of considerable analysis. With respect to the photon beam parameters, such analysis has generally fallen along one of two lines, study of either the axial profile of the beam when short pulses are of interest[4], and study of the transverse structure[5,6]. The theoretical analysis presented here pertains to the transverse optical field structure of tapered-wiggler oscillators.

Interest in the oscillator transverse field structure stems largely from the nonlinear interaction of the gain media and optical field. Geometries optimized for maximum electron-photon interaction will generally involve a long, small diameter e-beam centered in a larger photon beam. The resulting amplitude and phase modification of the photon beam, being radially nonuniform, leads to generation of optical cavity modes which should be accounted for in system design, and also leads to an output beam of lower quality than the ideal diffraction limit. It is the quantification of these effects that is pursued here.

The method of calculation is described in Sec. II. Phase and amplitude profiles of the photon field are determined in a plane perpendicular to the cavity axis, this plane being numerically propagated back and forth along the axis using a paraxial wave equation. Section III describes the application of this formalism to the FEL interaction and relevant geometries. The complexity of the FEL interaction is reduced by means of a resonant-phase approximation, thus providing a simple relationship between the phase of the stimulating and stimulated electric fields. While the calculations presented have relatively simple modal structure, the analysis is directly applicable to more complicated structure. The resonant-phase approximation does limit the applicability of the model to fully saturated photon intensity levels. The optical cavity is taken to be injected from an external source at the full saturated intensity, and the subsequent development of mode structure is the subject of primary interest. Actual tapered-wiggler FEL oscillators may be self started from spontaneous emission or require injection at or below saturation intensity. Our analysis method precludes modeling transverse mode structure effects in the small-signal start-up regime, but it provides a useful way to determine the steady mode structure in the saturated, trapped-particle regime of tapered-wiggler FEL oscillators. While the details of the mode structure during the approach to steady state will be dependent on the start-up method, the steady-state structure should be insensitive to the start-up method. The properties of the transverse field are analyzed by means of decomposition into Gaussian-Laguerre modes, providing a convenient measure of beam properties in terms of partition of the total power into modes. The mode structure

depends strongly on the degree of aperturing in the optical cavity, this resulting from finite size optical elements. Aperturing by the wiggler magnets will be particularly important in geometries optimized for FEL interaction strength[7]. Presence of the wiggler has been accounted for by truncation of the beam at positions of the beam corresponding to the wiggler entrance and exit locations. Results of the study are presented in Sec. IV and summarized in Sec. V.

## II. CALCULATIONAL METHODS

The free-electron laser oscillator is modeled using an axisymmetric physical optics code. Within the wiggler, the wave front is propagated numerically using a finite-difference solution of the paraxial wave equation [8]. For propagation between the wiggler and distant mirrors, the Huygens-Fresnel integral [9] is used. The computer model is used to find the transverse mode structure and far-field characteristics, accounting for diffraction, nonuniform gain media, refraction, and arbitrary mirror configurations and reflectivities.

A linearly polarized wave amplitude may be expressed as a scalar function of position and time

$$u(x,y,z,t) = U(x,y,z)\cos(\omega t + \Phi(x,y,z)), \quad [1]$$

where  $U$ ,  $\omega$ , and  $\Phi$  are the amplitude, angular frequency, and phase of the wave, respectively. Using phasor notation, the explicit time dependence may be removed

$$\hat{U} = U(x,y,z)\exp(-i\Phi(x,y,z)), \quad [2]$$

where we use the superscript " $\hat{\phantom{U}}$ " to denote a complex number, or phasor. The original time-dependent amplitude may be recovered by the transformation

$$u(x,y,z,t) = \text{Re}[\hat{U}(x,y,z)\exp(-i\omega t)]. \quad [3]$$

The complex wave amplitude propagates through free space according to the time-independent wave equation

$$\nabla^2 \hat{U} + k^2 \hat{U} = 0, \quad [4]$$

where  $k = 2\pi/\lambda$  is the laser wave number. For light traveling nearly parallel to the z-axis, one can remove most of the rapid phase variation by defining a new function  $\hat{\psi}$  by

$$\hat{U}(x, y, z) = \hat{\psi}(x, y, z) \exp(-ikz). \quad [5]$$

The function  $\hat{\psi}$  represents the difference between the actual wave front and a uniform plane wave, and thus is a much slower varying function of position. This function satisfies

$$\nabla^2 \hat{\psi} - 2ik \frac{\partial \hat{\psi}}{\partial z} = 0. \quad [6]$$

the so-called "paraxial wave equation". We solve this equation numerically in axisymmetric cylindrical geometry under the assumption that  $\hat{\psi}$  varies so slowly with z that its second derivative,  $\partial^2 \hat{\psi} / \partial z^2$ , may be neglected,

$$\frac{1}{r} \frac{\partial}{\partial r} \left[ r \frac{\partial \hat{\psi}}{\partial r} \right] - 2ik \frac{\partial \hat{\psi}}{\partial z} = 0. \quad [7]$$

This free-space propagation equation is solved implicitly using a centered-difference technique involving inversion of a tridiagonal matrix[10]. This method is stable independent of step size, thus allowing the step size  $\Delta z$  to be chosen on the basis of desired accuracy, rather than on stability considerations. The technique is second-order accurate and is found to achieve excellent energy conservation.

A disadvantage of the finite-difference propagation technique is the inability to accurately treat sharp aperture edges. At an aperture, the complex amplitude is discontinuous, so that high order radial derivatives

are undefined. Truncation errors due to these terms cannot be made arbitrarily small by decreasing  $\Delta r$ . This difficulty is overcome by using smoothly tapered aperture edges[8], allowing accurate numerical calculation of the diffraction pattern. The distinction between smooth and hard apertures is unimportant to this application because differences in the fields are found only at locations very close to the aperture[11]. The apertures are smoothed by using a Gaussian profile at the edge. For example, the mirror reflectivity is

$$R(r) = \begin{cases} R_0 & r < r_0 \\ R_0 \exp\left[-(r-r_0)^2/\tau^2\right] & r > r_0, \end{cases} \quad [8]$$

where  $r_0$  is the radius of the portion of the mirror with uniform reflectivity,  $R_0$ , and  $\tau$  is the truncation distance. We choose  $r_0$  and  $\tau$  so that the actual diameter,  $2a_m$ , of the mirror being modeled lies at the half power points of the Gaussian edges.

In regions of the problem where the FEL gain medium is active, the propagation equation contains an additional term describing the FEL interaction

$$\frac{1}{r} \frac{\partial}{\partial r} \left[ r \frac{\partial \hat{\psi}}{\partial r} \right] - 2ik \left[ \frac{\partial \hat{\psi}}{\partial z} - Af(r) \frac{\hat{\psi}}{|\hat{\psi}|} e^{-i(\pi/2 - \theta)} \right] = 0. \quad [9]$$

Here parameters  $A$  and  $\theta(r, z)$  describe the E-field generated by the gain medium. The parameter  $A$  is the amplitude of the E-field generated on-axis, per unit distance along the wiggler (i.e., an interaction of length  $dz$  generates a field of amplitude  $A dz$ ).  $A$  is proportional to the density of trapped electrons. Since the number of electrons in the bucket is fixed,  $A$  is independent of axial position. The variation in gain along the wiggler length is due to the variation of the phase  $\theta$  of the stimulated field (the field of amplitude  $A dz$ ) with respect to the stimulating field,  $\hat{\psi}$ . Phases of +90 and -90 degrees correspond to gain and absorption, respectively, with no phase shift. Phases of 0 and 180

degrees correspond to phase-front lag and advance, respectively, with no gain. The dimensionless  $f(r)$  is a spatial form factor describing the radial electron density profile.

The gain term is included explicitly in the wave-front propagation algorithm using an iterative procedure to achieve centered differencing and second-order accuracy. The propagation algorithm is solved on a uniform two-dimensional grid with about 200 steps in the radial direction and 100 steps in the axial direction. The problem is solved by specifying an initial wave front at a particular axial position, and then using the propagation algorithm to advance the wave front forward in  $z$  simultaneously at each radial position. When necessary, due to a more rapidly varying complex electric field, the axial grid is subdivided locally.

Several checks confirm the accuracy of the finite-difference propagation algorithm. Control calculations have been made using different grid sizes. These calculations verify that the results are independent of grid size, for the grid resolution used in this study. Furthermore, the beam power is conserved to within 0.05 percent when a combination of  $TEM_{00}$  and  $TEM_{10}$  modes is propagated for 35 round trips around an unapertured confocal resonator.

### III. APPLICATION TO FEL GEOMETRIES

The FEL cavity geometry is shown in Fig. 1.

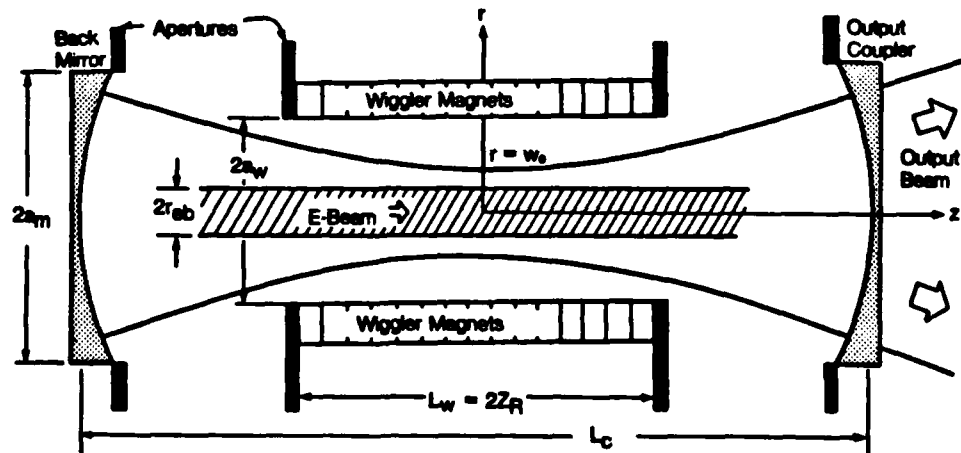


Figure 1. Schematic of axisymmetric FEL oscillator geometry. Radial dimension is greatly exaggerated for clarity.  $Z_R = \pi w_0^2 / \lambda$ .

A plane-polarized optical beam is circulated in a symmetric stable resonator. The wiggler length is equal to two Rayleigh ranges of the optical beam. This geometry produces a shallow waist at the wiggler center, and nearly optimizes the electron-photon energy exchange. The majority of calculations presented in this paper pertain to confocal cavities, in which case the mirrors are located precisely at the ends of the wiggler. In practice, the mirrors may be separated by more than the wiggler length to provide e-beam access, but the basic aspects of the problem remain the same. The cavity mirrors have a radius of  $a_m$ . The presence of the wiggler magnets is accounted for by including additional apertures of radius  $a_w$  at each end of the wiggler. For the following analysis, the mirror on the right is taken to be a partially reflective output coupler, with radially independent reflectivity. The output coupling is chosen to be approximately equal to the FEL gain at saturation. Low to moderate gain, less than 50 percent per pass, is considered in all cases. The electron beam is assumed to have a Gaussian radial electron density profile

$$f(r) = \exp\left[-r^2 / r_{eb}^2\right], \quad [10]$$

independent of axial position. In all calculations presented, the e-beam is assumed to be fairly small in diameter compared to the photon beam.

Calculation of the interaction with the gain medium is based on the synchronous-particle approximation. That is, all interacting electrons are assumed to be trapped in the ponderomotive potential well, and it is further assumed that all such electrons are located in the well at the stable-phase point[2]. This in turn determines the relative phase between the locally generated field and locally applied field, with the result that  $\theta$  in Eq. [9] can now be replaced with the stable-phase angle. This approximation is useful since trapped electrons oscillate about the synchronous-phase point, but its use precludes modeling effects associated with the pendulum motion of trapped particles.

The stable-phase angle,  $\theta$ , is a function of the local electric field and local wiggler taper  $d\gamma_r/dz$ , where  $\gamma_r$  is the resonant energy. The wiggler taper must be specified as an input parameter. For this analysis, the taper is chosen so that, in the presence of a  $TEM_{00}$  photon beam, the phase would be independent of axial position. In the presence of the FEL interaction, however, the wave front is typically not pure  $TEM_{00}$ . The phase angle is therefore not constant, but is specified in terms of the local field  $\hat{U}(r,z)$  by

$$\sin\theta(r,z) = \sin\theta_0 \frac{|U_{0,0}(0,z)|}{|U(r,z)|} = \frac{\sin\theta_0}{|U(r,z)|} \frac{1}{\sqrt{1 + [z/Z_R]^2}}, \quad [11]$$

where  $Z_R = \pi w_0^2/\lambda$ ,  $w_0$  is the 1/e E-field radius of the  $TEM_{00}$  beam at the waist,  $|U_{0,0}(0,z)|$  represents the on-axis amplitude of a  $TEM_{00}$  beam normalized for unity amplitude at the waist, and  $\theta_0$  is the stable-phase angle which would be produced on axis in the presence of a  $TEM_{00}$  beam of this normalization. The initial pump beam is a  $TEM_{00}$  wave with unity normalization. As the modal structure evolves due to the FEL interaction, the resonant phase evolves self-consistently according to Eq. [11]. Relatively high E-field values cause the electrons to slide toward the bottom of the bucket (toward small phase angles with high refraction and low gain) while relatively small E-fields cause large phase angles and high gain. This effect tends to produce an equilibrium value of intracavity flux.

In principle, the phase angle varies radially within the e-beam. Such variation has been included, but is unimportant for the cases examined since the photon intensity is nearly constant across the e-beam. If the phase angle reaches 90 degrees, electron detrapping, or escape from the ponderomotive potential well and subsequent loss of energy exchange, will occur. We have allowed electron detrapping to occur as a result of radial variation in the photon intensity distribution, but this is also unimportant for these cases. The code treats detrapping by assuming straight-line electron trajectories parallel to the wiggler axis. This

neglects the sinusoidal betatron orbits [12] which result from transverse gradients in the magnetic field. The code is nevertheless applicable to cases which have significant betatron motion, provided that there is little radial variation of photon intensity and phase across the e-beam.

Detrapping may also occur across the entire e-beam as a result of mode beating. For example, it is shown later that interference between the 1-0 and 0-0 modes can lead to axial intensity fluctuations of roughly a factor of two. If a design phase angle of  $\theta_0 = 45$  degrees had been chosen, Eq. [11] shows that detrapping would occur on axis when the competition of the two modes is included. Since  $\theta(r,z)$  is calculated based on the local field, any detrapping caused by mode beating is self-consistently taken into account. The detrapping problem can be avoided by choosing a smaller design value of the phase angle, but at the expense of electron deceleration.

The oscillator mode structure may be characterized by decomposing the wave front into the axisymmetric Gaussian-Laguerre modes of the resonator. The normalized, orthogonal modes may be written[9]

$$\hat{U}_{p,0}(r,z) = \sqrt{\frac{2}{\pi}} \frac{1}{w(z)} \exp\left[-\left(\frac{r}{w(z)}\right)^2\right] L_p\left[2\left(\frac{r}{w(z)}\right)^2\right] \cdot \exp\left[-i\left\{kz - (2p+1)\tan^{-1}\left(\frac{z}{Z_R}\right) + \frac{z}{Z_R}\left(\frac{r}{w(z)}\right)^2\right\}\right] \quad [12]$$

where  $w(z) = w_0\sqrt{1 + (z/Z_R)^2}$ ,  $p = 0, 1, 2, \dots$  is an integer index for each mode, the  $L_p$  are the associated Laguerre polynomials of order  $p$ , and  $Z_R = \pi w_0^2/\lambda$  is set by the mirror curvature. The modes  $\hat{U}_{0,0}$ ,  $\hat{U}_{1,0}$ ,  $\hat{U}_{2,0}, \dots$  correspond to circular  $TEM_{00}$ ,  $TEM_{10}$ ,  $TEM_{20}, \dots$  modes, respectively. As the modes propagate through one round trip of the cavity, they incur a phase shift relative to a plane wave of  $4(2p+1)\tan^{-1}(L/2Z_R)$  due to curvature.

We can describe any arbitrary wave front as an expansion of modes

$$\hat{U}(r,z) = \sum_{p=0}^{\infty} \hat{a}_p \hat{U}_{p,0}(r,z) \quad . \quad [13]$$

The complex coefficients are conveniently found by evaluating

$$\hat{a}_p = \int_0^{\infty} \hat{U}(r,z) \hat{U}_{p,0}^*(r,z) 2\pi r dr \quad , \quad [14]$$

where the superscript "\*" denotes a complex conjugate. On each pass through the laser the wave-front mode structure is analyzed at the output mirror, immediately following the mirror truncation. This decomposition describes both the internally reflected and the outcoupled field. The far-field distribution may be found by passing the output beam through a collimating lens, then focusing with a spherical mirror. A Huygens-Fresnel integral[9] is used for propagation to the focal spot, yielding the far-field pattern.

Most of the simulations presented here pertain to confocal cavities, that is the Rayleigh range  $Z_R$  is equal to half the cavity length,  $L_C$ . Confocal systems, as well as concentric ( $L_C/Z_R = \infty$ ) and planar ( $L_C/Z_R = 0$ ), can support unusual mode structure because the relative phase slippage between cavity modes over one round trip is an integral multiple of  $2\pi$ . For empty cavities, relative phases of individual modes at any given transverse plane will repeat on each round trip. Consequently, the mode mixing due to truncation by any apertures present has interesting properties. For example, the gain-free confocal system injected with pure 0-0 mode develops almost no 1-0 mode by way of mirror truncation, but the amount of 2-0 mode can be appreciable. The 1-0 mode is produced by truncation of the 0-0 mode at each mirror, but the 1-0 fields generated at the two mirrors drive 1-0 modes which are 180 degrees out of phase. The 2-0 mode fields produced at each mirror are in phase. If 1-0 mode is produced by the gain media, another interesting effect occurs. In

propagating from one end of the cavity to the other, the phase of the 0-0 mode changes by  $\pi/2$  (relative to a plane wave), while that of the 1-0 mode slips by  $3\pi/2$ . The interference is therefore different at each end of the cavity, providing an asymmetry in the axial direction. Such an asymmetry can be supported in the FEL since the gain mechanism is active in one direction only.

These effects are less apparent in cavities intermediate to the special cases of confocal, concentric, or planar. The importance of any deleterious effects might therefore be considered minimal, but the reverse may actually be true. The low Fresnel number and small wiggler bores inherent to FELs tend to result in unusually high energy loading on mirror surfaces. For high average power systems, alleviation of these problems may require the use of very long, near-concentric cavities.

#### IV. RESULTS

##### 4.1 Properties of a Confocal FEL Resonator

The mode structure of the confocal FEL oscillator described in Table I has been investigated in detail. We will first point out some of the basic features of the mode structure of a confocal FEL oscillator, followed by an investigation of the effect of varying some of the parameters.

The conditions listed in Table I describe a confocal stable resonator with apertures of radius  $1.8 w$ , where  $w$  is the  $1/e$  radius of the E-field of a  $TEM_{00}$  mode at the ends of the wiggler.

TABLE I

Standard Conditions for FEL Oscillator  
Mode Structure Investigation

Cavity Length, $L_C/Z_R$	2 (confocal)
Aperture Size, $a_w/w$	1.8
E-Beam Size, $Z_R/Z_R^{eb}$	10
Design Phase Angle, $\theta_0$	20.7°
Gain	10%/pass
Output Coupling	9.1%
Aperture Truncation Length, $T/a_w$	0.055

This mirror size provides a modest degree of mode selection. Higher order modes are attenuated since they carry more energy at larger radii. The electron beam size is specified by  $Z_R/Z_R^{eb} = 10$ , where we define  $Z_R^{eb} = \pi r_{eb}^2/\lambda$  to be the Rayleigh range based on the 1/e radius of the Gaussian e-beam. We choose the electron beam size to be significantly smaller than the pump beam ( $r_{eb}/w_0 = 0.316$ ), so the e-beam is essentially pumped by a uniform intensity wave front. The peak (on-axis) electron density is chosen to give a gain approximately equal to the 9.1 percent output coupling (reflectivity of 0.909). Small additional cavity loss results from clipping at the apertures.

The distribution of Gaussian-Laguerre modes at the output coupler are shown as a function of round-trip number in Fig. 2. The wave front is initiated as a  $TEM_{00}$  mode, but settles down within 30 passes to a steady mode distribution containing a significant contribution of 1-0 mode. All higher modes are strongly suppressed by the finite aperture radii. The high content of 1-0 mode is due to the FEL interaction, rather than by truncation at the apertures. The fraction of 1-0 mode power in the absence of gain is only  $2.6 \times 10^{-6}$ . The higher order mode with the highest energy content in the bare resonator is the 2-0 mode; it constitutes only 0.27 percent of the total power.

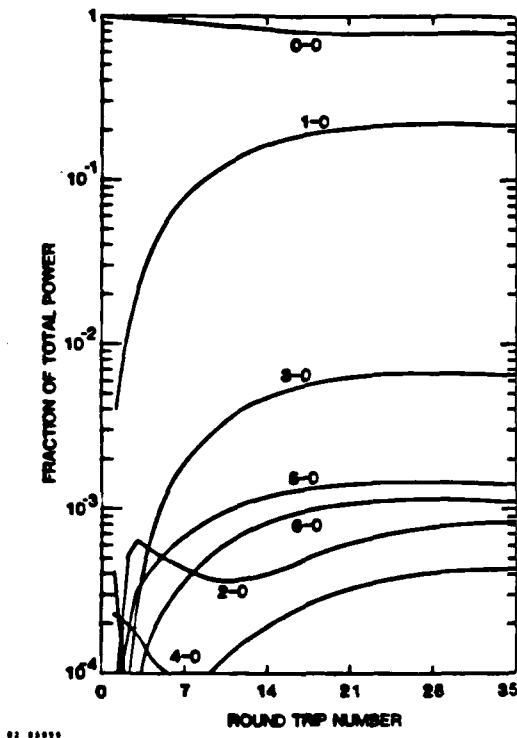


Figure 2. Mode structure evolution for conditions of Table I.

The electron trapping fraction and beam power are shown as a function of round-trip number in Fig. 3.

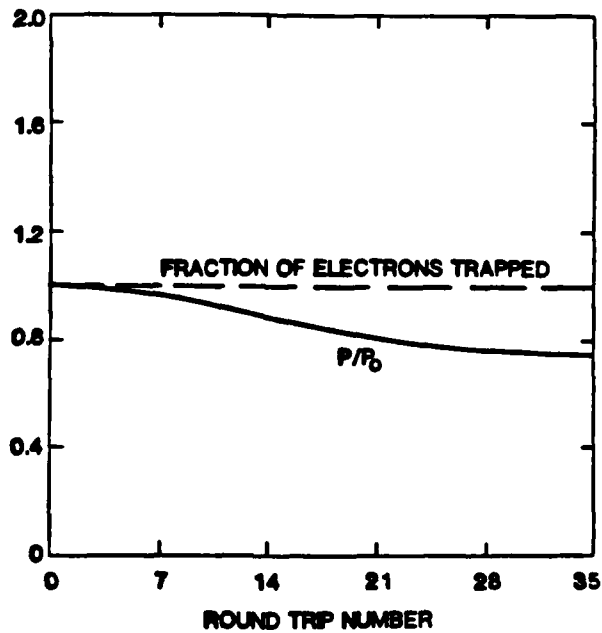


Figure 3. Beam power and fraction of electrons trapped as a function of round-trip number for conditions of Table I.

As the mode structure evolves, the round-trip losses exceed the gain slightly on each pass, allowing the power level to decay about 25 percent. Once a steady mode structure has developed, the power level comes to steady state as the phase angle adjusts to allow the gain to match the round-trip losses. The electron beam is trapped essentially over its full radius.

The steady-state phase angle of the FEL interaction is shown as a function of axial and radial position in Fig. 4.

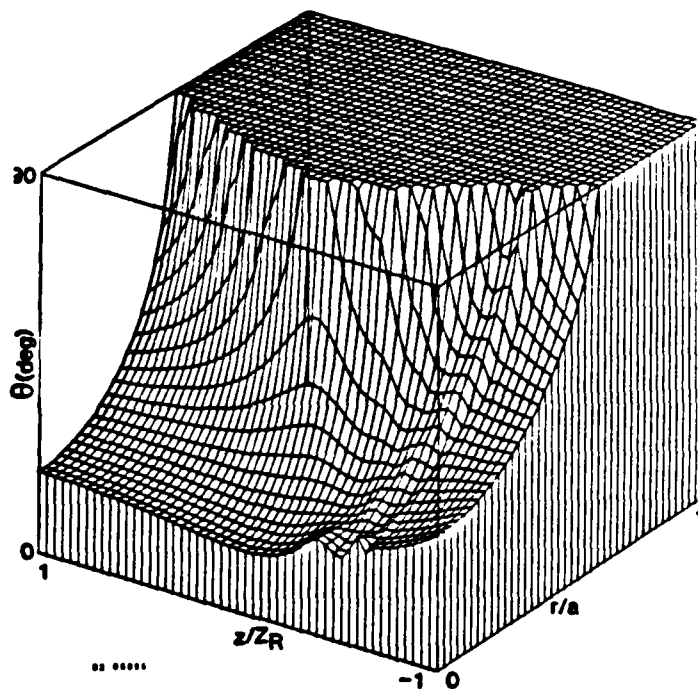


Figure 4. Steady-state phase angle for FEL interaction as a function of position. Conditions given in Table I.

While the on-axis phase angle is initially 20.7 degrees for the 0-0 mode pump beam, the steady mode distribution results in on-axis phase angles which vary between 15 and 32 degrees. The largest on-axis phase angle, or lowest intensity, occurs at the back mirror. The radial phase angle profiles have a rather broad, flat distribution, with a sharp transition to large angles and detrapping at large radius. The broad distribution is consistent with the e-beam being pumped by an essentially uniform intensity wave front. The narrowest profile occurs at the midplane between the mirrors (at the photon beam waist) where detrapping occurs at  $r = 2.4 r_{eb}$ . Downstream from this point, all electrons at this radius or

greater are detrapped, but this constitutes only about 0.3 percent of the total e-beam.

The steady intracavity intensity distribution is illustrated in Fig. 5.

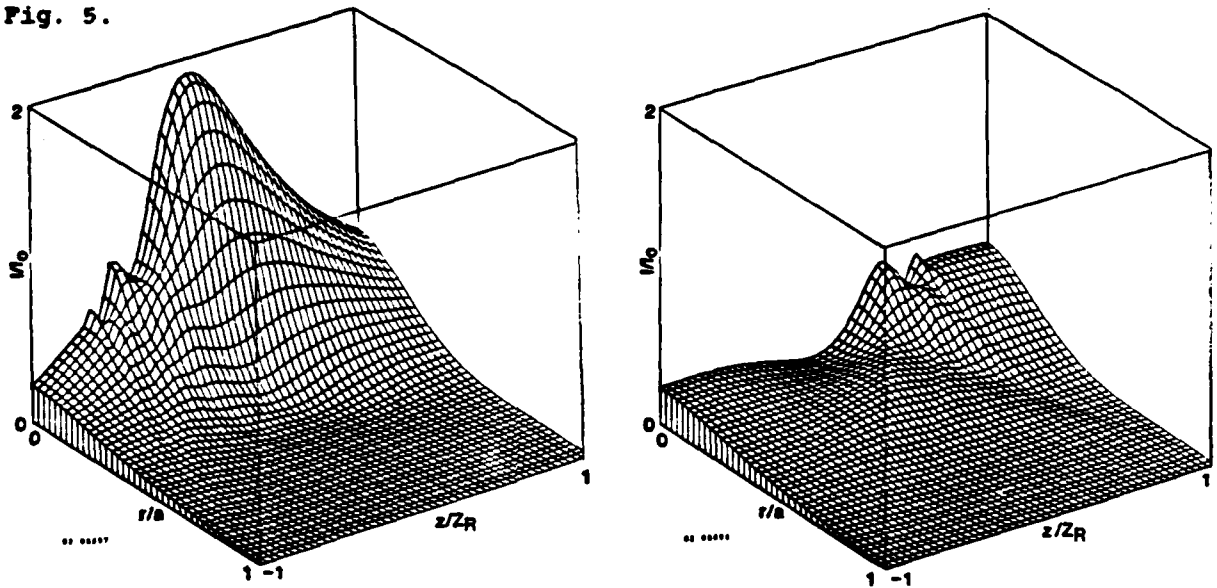
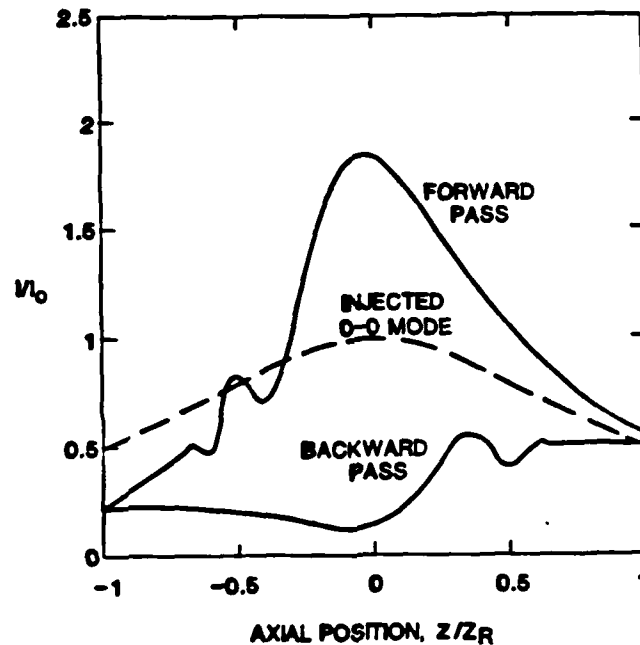


Figure 5. Intracavity intensity distributions of steady mode structure on (a) forward pass, and (b) return pass for conditions of Table I.

The intensity distribution  $I(r, z)$  for the forward pass is shown in Fig. 5(a) and the backward pass in 5(b). The intensity is normalized in such a way that the on-axis intensity for the injected 0-0 mode is 1 at the midplane ( $z/Z_R = 0$ ) and 0.5 at the mirrors ( $z/Z_R = \pm 1$ ). The sharp variation of intensity near the axis just after a mirror reflection is due to the diffraction pattern of the aperture. The steady distribution develops in such a way that the central on-axis intensity is higher than that of the individual 0-0 mode pump beam on forward passes and lower on backward passes. The forward and backward going on-axis intensities are compared with the 0-0 mode in Fig. 6.

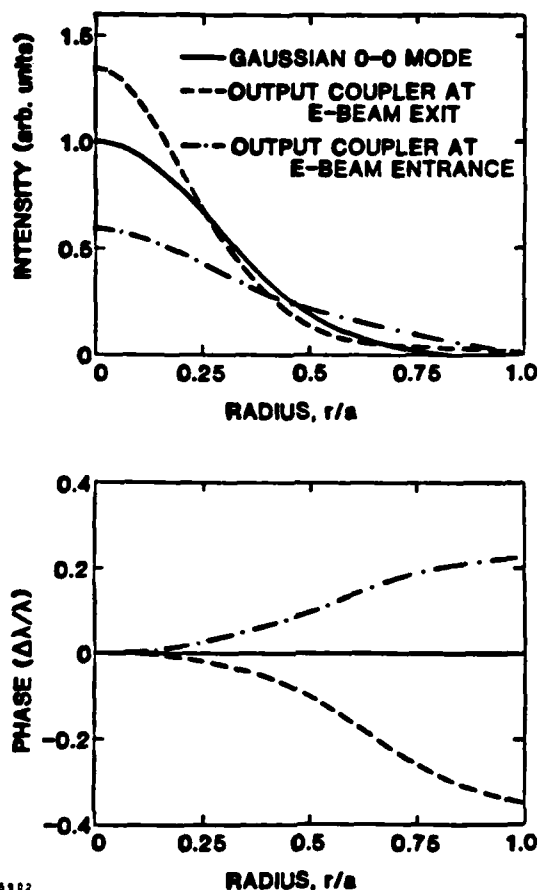


82 85901

Figure 6. Comparison of on-axis intensity distributions of steady mode structure and injected 0-0 mode.

The on-axis intensity on the output mirror is over two times that of the back mirror. This difference cannot be accounted for by gain, which is only 10 percent, but results from interference between the dominant 0-0 and 1-0 modes. The relative phases of the two modes are such that they constructively interfere on-axis on forward passes and at the output mirror while destructively interfering on backward passes and at the back mirror.

The radial structure of the output beam is shown by the intensity and phase profiles in Fig. 7.



02 0502

Figure 7. Intensity and phase profiles at output coupler for conditions of Table I. Phase profile has spherical curvature of output mirror removed. Intensity profiles are normalized for equal power.

The conditions are those of Table I, except that data is included for outcoupling at either end of the cavity. The axial structure and Gaussian-Laguerre mode content of the two cases is essentially identical; the differences in the intensity and phase profiles may be attributed to different relative phases between the 0-0 and 1-0 modes. When the spherical curvature of the output mirror is removed from the phase distributions of the two nearly Gaussian output beams, each beam contains some additional residual spherical curvature. Evidently the beam at the

e-beam exit has somewhat more spherical curvature than the output mirror and the beam at the e-beam entrance has somewhat less curvature.

A useful measure of the focusability of the beams is made by examining their amplitude-weighted rms phase deviations at the output mirror. When all spherical curvature is removed from the phase profiles, the residual phase aberrations shown in Fig. 8 are found.

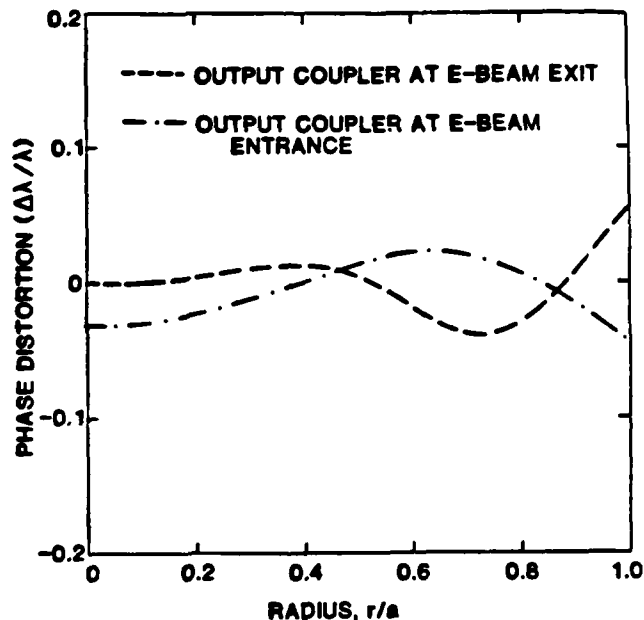


Figure 8. Residual wave-front distortion at output mirror with all spherical curvature removed.

All phase differences across the aperture are less than 1/10 of a wavelength. Since the aberrations are predictable rather than random, they could be corrected by use of properly designed optical components. Such an effort is probably unnecessary, however, since the aberrations are so small. The amplitude-weighted rms wave-front distortion[13] is approximately 1/50 of a wavelength at both the e-beam exit and entrance. This phase deviation results in a far-field peak intensity loss of less than 2 percent. Equivalently, the Strehl ratio is greater than 98 percent.

An additional demonstration of output beam quality is the calculation of power delivered to a far-field target. Conceptually, such a test is made using the laser together with a focusing lens. An appropriate figure of merit is the power which can be delivered within a specified target area using a lens of specified aperture size. A nearly equivalent mathematical figure of merit involves the fraction  $\eta$  of total power  $P_{TOT}$  which can be delivered within a radius  $R_t$  on the target

$$\eta = \frac{1}{P_{TOT}} \left( \frac{f}{\alpha} \right)^2 \int_0^{R_t} I(r) 2\pi r dr. \quad [15]$$

Here  $f$  is the distance from focusing lens to target, and  $\alpha$  is the mean radius of the beam as it exits the focusing optics.

$$\alpha = \frac{1}{P_{TOT}} \int_0^{\infty} r I(r) 2\pi r dr. \quad [16]$$

Results are shown in Fig. 9 as a function of the target radius. The target radius has been normalized to  $\alpha/f$ .

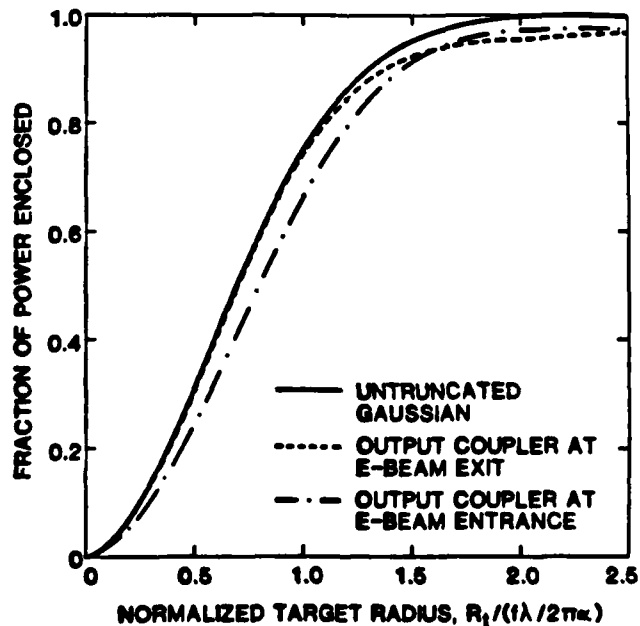


Figure 9. Fraction of power enclosed at focal plane as a function of normalized radius.

Results for a diffraction-limited TEM<sub>00</sub> beam are included for comparison. The difference in power delivered to the target for these two output beams is very small. The high focusability of each beam is evident.

Such a conclusion may appear to contradict the mode decomposition of Fig. 2, which shows about 20 percent of the energy to be in the 1-0 mode. The apparent discrepancy lies in the fact that Fig. 2 is a decomposition based on the basis set determined by the mirror geometry. The choice of different basis sets, i.e., a change of Rayleigh range and waist location, will result in different energy partitions. We have made an empirical search of Rayleigh range and waist location parameters for the purpose of finding the highest projection into the 0-0 mode. The result, for the case of outcoupling at the e-beam exit, is that 96.7 percent of the total energy can be projected into the 0-0 mode using the best matched Rayleigh range and waist location. Physically, this means that the intracavity beam is of nearly diffraction-limited quality, but its curvature is not matched to that of the fundamental cavity mode. The mismatched wave front does not reflect back on itself, resulting in the front-to-back asymmetry.

#### 4.2 Parametric Variation

We have seen that for a nominal phase angle,  $\theta_0$ , of 20.7 degrees, approximately 22 percent of the total energy of the stable transverse mode lies in the 1-0 cavity mode. The phase angle is a design parameter, depending primarily on the wiggler taper, cavity Q, and e-beam current. Analysis of the mode structure variation as a function of  $\theta_0$  is of interest, since a range of design values will be achievable in practice. This has been investigated with two simulations in which phase angles of 90 degrees and 0 degrees were used. These two limiting cases correspond to pure gain and pure refraction, respectively. In both cases, the phase angle was fixed everywhere in x and z so that there is no possibility of electron detrapping. All other parameters are those of Table I. The results are shown in Fig. 10.

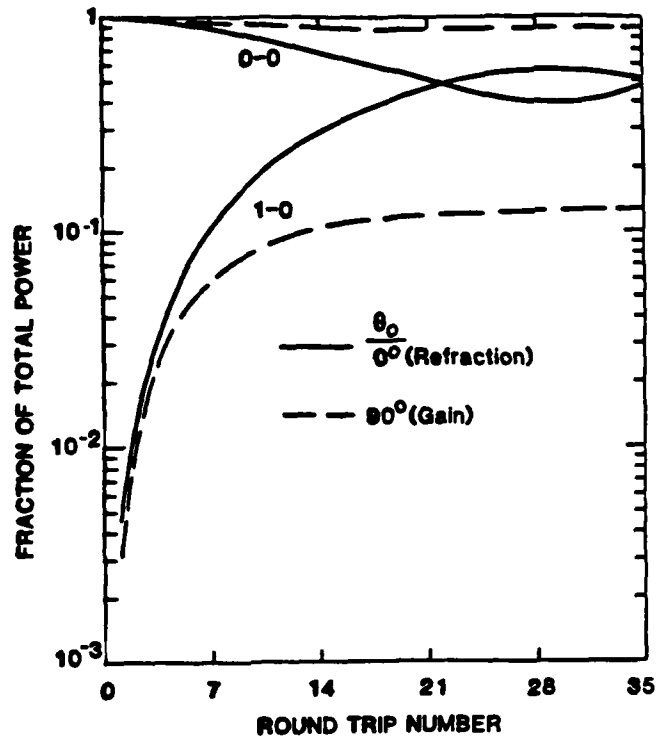


Figure 10. Mode structure evolution for various FEL interaction phase angles with fixed trapped electron density. Phase angle is everywhere uniform with no electron detrapping.  $Z_R/Z_R^{eb} = 10$ ,  $a_w/w = 1.80$ ,  $L_C/Z_R = 2$ .

When compared to the earlier results, the pure refraction case develops a large fraction of higher order modes. In fact, the round-trip diffraction losses, i.e., power falling outside the mirror radius, approach 10 percent. Evidently, refraction is a much stronger mechanism for beam spreading than gain. While large phase angles appear to be desirable for minimizing the higher mode content, there are fundamental limitations on how large a design phase angle can be used. For example, as discussed in Sec. III, larger design phase angles are more susceptible to detrapping due to mode beating.

This variation in phase angle was made with a fixed trapped electron density. It could be achieved in practice by variation of the cavity  $Q$ , thereby changing the cavity flux level and rotating the locally generated electron E-field phasor with respect to the applied E-field phasor. A related variation is the change in length of the electron E-field phasor with the angle fixed.

Results are shown in Fig. 11.

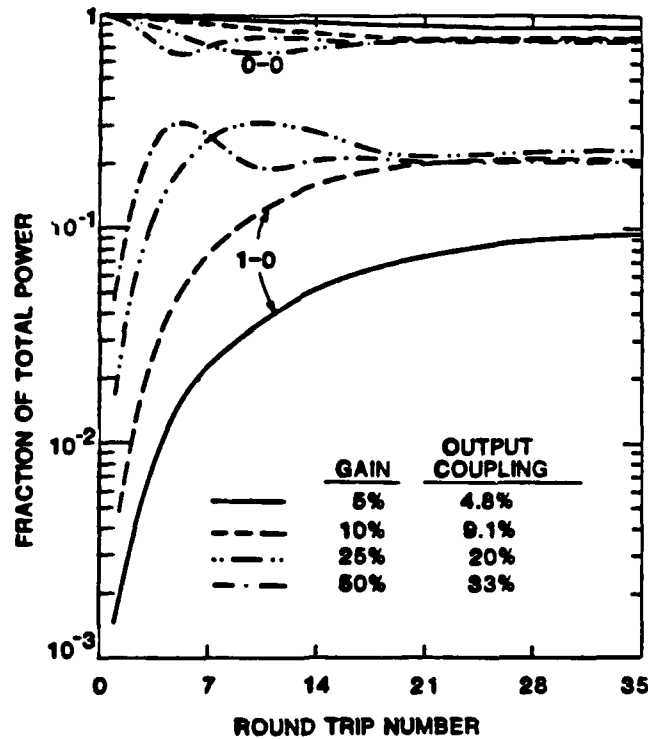


Figure 11. Mode structure for various output couplings with fixed phase angle.  $\theta_0 = 20.7^\circ$ ,  $Z_R/Z_R^{eb} = 10$ ,  $a_w/w = 1.80$ ,  $L_c/Z_R = 2$ .

In this case, use of low output coupling results in a general reduction in higher order mode content, since both gain and refraction are reduced. As the gain is increased above 10 percent, the content of 1-0 mode appears to reach a plateau. Apparently, there is a mechanism for either increasing the losses of 1-0 mode or decreasing its production, causing the 1-0 mode content to saturate at a level independent of the length of the electron E-field phasor.

The effect of changing the electron-beam size with fixed gain is shown in Fig. 12.

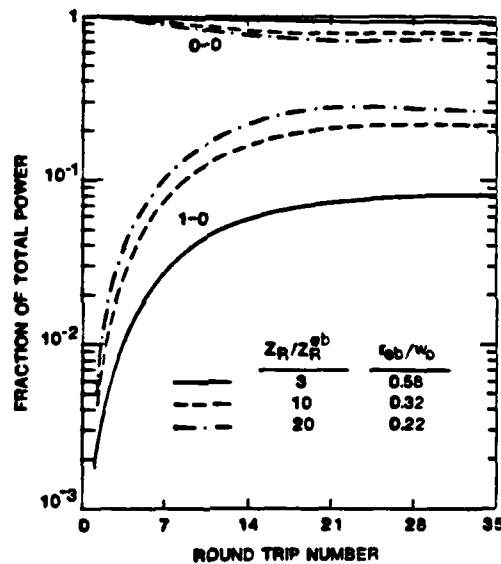


Figure 12. Mode structure for various e-beam sizes with fixed gain. Gain = 10 percent, 9 percent output coupling,  $\theta_0 = 20.7^\circ$ .  $a_w/w = 1.80$ ,  $L_c/Z_R = 2$ .

As the e-beam diameter is varied, the trapped electron density is changed so as to keep the gain constant. The e-beam size is not increased to the point that detrapping of the wings of the e-beam density distribution becomes significant. Increasing the size of the e-beam decreases the content of higher modes. This is consistent with the notion that a small diameter gain media leads to high diffraction angles and hence high order modes. However, in this case, the e-beam constitutes an antenna of sufficient length that the angular spread of its emission is nearly length

dominated and independent of transverse size. Accordingly, we expect that reduction of the e-beam size to zero will not produce mode structure dramatically different from that of the  $Z_R/Z_R^{eb} = 20$  curve of the figure.

The steady-state mode structure is also a function of the aperture size. As shown in Fig. 13, the use of small apertures strongly suppresses higher order modes.

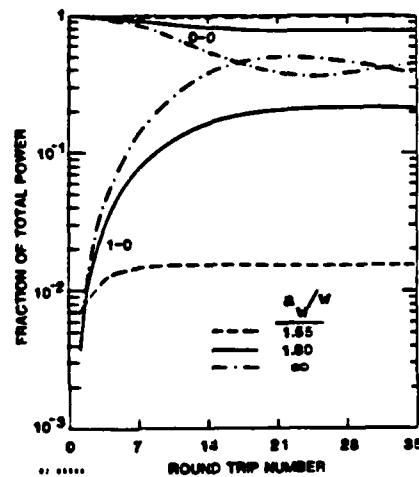


Figure 13. Mode structure for several aperture sizes.  $\theta_0 = 20.7^\circ$ , 10 percent gain, 9 percent output coupling,  $Z_R/Z_R^{eb} = 10$ ,  $L_C/Z_R = 2$ .

The diffraction losses, defined as the fraction of the beam power falling outside the mirror radius, actually decrease for the smaller mirror size. The round-trip fractional diffraction loss is 0.0310 for  $a/w = 1.80$  and 0.0221 for  $a/w = 1.55$ . Apparently there is a finite aperture size for which the diffraction losses are minimized. For the infinite mirror size there is no mode selection, since the output coupling is mode independent. In this case, it is interesting to note that the relative content of 0-0 and 1-0 modes oscillates.

The last variation considered is that of cavity length. As discussed in Sec. III, mode beating in confocal and concentric cavities

has special properties since the round-trip phase slippage between modes is an integer multiple of  $2\pi$ . This is seen in Fig. 14 where confocal and concentric cavities support large fractions of  $TEM_{10}$  mode, but for intermediate cavity lengths the fraction of 1-0 mode decreases dramatically.

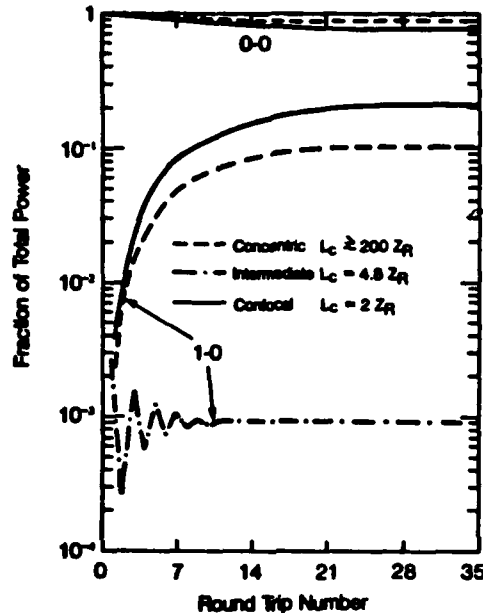


Figure 14. Mode structure for various cavity lengths,  $\theta_0 = 20.7^\circ$ ,  $Z_R/Z_R^{eb} = 10$ ,  $a_w/w = 1.80$ ,  $a_m/w = 3$ , gain = 10 percent, 9 percent output coupling.

It was shown previously (Fig. 6) that the presence of higher order modes has unusual effects on the intensity distribution within the wiggler. In the case of the concentric cavity, the optical beam, when compared to the fundamental cavity mode, is relatively broad and low intensity where it enters the wiggler. Before exiting the wiggler, the beam then focuses to a relatively narrow, intense waist. This is analogous to the behavior seen on forward passes in the confocal cavity (see Fig. 6). But in contrast to the confocal results, the spot sizes on the two mirrors and the intensity distributions on forward and reverse passes are very similar in the concentric cavity.

The lack of higher order mode content in cavities of intermediate length results from the phase of the 1-0 mode being determined by the

ponderomotive potential, which is formed by the dominant 0-0 mode. Thus, the 1-0 phase is tied to the 0-0 mode, and the 1-0 wave produced on a given round trip is not in phase with 1-0 waves produced on earlier or subsequent round trips in a cavity of intermediate length. A further manifestation of the varying phase relationship between modes is that the intensity distribution on the mirrors, and hence, the cavity losses, are variable from one round trip to another. This results in the ripple seen in Fig. 14.

Nevertheless, a steady mode structure develops which has a constant relative phase between any two modes at any given location on any pass. This is because the production of higher order modes, either by mirror truncation or FEL gain and refraction, always occurs at a constant phase angle relative to the existing pump beam (i.e., coherently). The higher order mode which is produced (say 1-0 mode, for example) will continue to undergo phase slippage relative to the 0-0 mode as it propagates around the cavity. However, it is also gradually attenuated and during its lifetime it has a fixed phase relative to the 0-0 mode at any given location.

Of the three cavity lengths considered, the confocal and concentric cavities have the highest content of higher order modes. The round-trip diffraction losses are also highest for these cavities, as indicated in Table II.

**Table II**  
**Round-Trip Aperture Losses for**  
**Various Cavity Lengths**

<u>Cavity Length, <math>L_c/Z_R</math></u>	<u>Round-Trip Fractional</u> <u>Diffraction Loss</u>
≥ 200	0.036
4.8	0.009
2	0.031

These losses pertain to energy passing beyond the edges of the mirrors and energy lost due to aperturing by the wiggler magnet or other elements in the beam line. For the confocal and concentric cases, the loss is about one-third of the output coupling, representing relatively inefficient energy extraction.

#### V. SUMMARY AND CONCLUSIONS

The transverse structure of the tapered-wiggler FEL optical field has been analyzed by numerical solution of a paraxial wave equation. The optical cavity is initially injected from an external source at its full saturated intensity and the subsequent transverse structure evolution is of interest. Unusual features of the FEL geometry, as compared to conventional lasers, include the narrowness, or more precisely the low Fresnel number of the gain media, the small diameter of the gain media with respect to that of the optical field, and the lack of gain on return passes. These factors tend to produce a steady-state mode structure different from the pure  $TEM_{00}$  injected wave.

The higher order mode content is especially evident in confocal and near-concentric optical cavities, i.e., those with mirrors separated by one or two times their radius of curvature. For such cavities, the round-trip phase shift between modes is an integer multiple of  $2\pi$ , a special situation resulting in constructive addition of higher order modes produced on different round-trips. The presence of higher order modes can significantly affect the photon beam shape, providing unusual effects. For example, in the confocal cavity case, the beam exhibits different radial structure on forward and reverse passes, as well as different spot sizes on the front and rear mirrors. Practical FEL's operating at substantial average power levels are likely to require near-concentric cavities in order to provide sufficiently large spot sizes at the mirrors. In this case,  $2\pi$  shift occurs between the dominant  $TEM_{00}$  and

TEM<sub>10</sub> modes in one pass, rather than a round trip, so that spot sizes on the front and rear mirrors and forward and reverse propagating waves differ from those of the fundamental mode but are comparable to each other.

The quality of the output beam is excellent for the cases studied, being of nearly diffraction-limited quality. This result is somewhat surprising in view of the TEM<sub>10</sub> mode content which complicates the intracavity structure. This apparent contradiction may be understood by noting that the intracavity wave-front curvature is not matched to that of the fundamental mode of the cavity, while the intracavity beam is essentially diffraction limited.

Additional findings involve the choice of synchronous phase angle, a parameter chosen, within limits, at the discretion of system designers. It is found that for a given electron density, a synchronous phase angle chosen to maximize gain results in much less TEM<sub>10</sub> (or higher order) mode production than does a phase angle chosen to maximize the phase shift. In the former case, the e-beam acts as an extended antenna which produces a field much like that already in the cavity, while in the latter case, the e-beam acts like a series of focusing lenses.

A useful application of the techniques described would be analysis of the effects of hole coupling as a means of output coupling in cavities compatible with high average power. Extension of these techniques to include the unbunched nature of electrons entering the wiggler and subsequent oscillation of the phase angle in the ponderomotive potential well, would be useful. A related effect of interest is the slippage of photons relative to electrons when short pulses are considered. In this case, the transverse structure is modified due to reduction of the effective interaction length.

**Acknowledgements**

The authors wish to thank Dr. D.D. Lowenthal of Mathematical Sciences Northwest, Inc., for several helpful discussions.

This research was supported by AFOSR Contract Number F49620-81-C-0079 and DARPA Contract Number ONR: N00014-80-C-0443.

## References

1. D.A.G. Deacon, L.R. Elias, J.M.J. Madey, G.J. Ramian, H.A. Schwettman, and T.I. Smith, Phys. Rev. Lett. 38, 892 (1977).
2. See for example, N.M. Kroll, P.L. Morton, and N.M. Rosenbluth, "Enhanced Energy Extraction in Free-Electron Lasers by Means of Adiabatic Decrease of Resonant Energy," in Physics of Quantum Electronics 7, Editors S.F. Jacobs, H.S. Pilloff, M. Sargent, M.O. Scully, and R. Spitzer, (Addison-Wesley, Reading, Mass., 1980), p. 113.
3. Tapered wiggler verification experiments in progress include those at Los Alamos National Laboratory, Mathematical Sciences Northwest, Inc. and TRW.
4. See for example, W.B. Colson and S.K. Ride, "The Free-Electron Laser: Maxwell's Equations Driven by Single-Particle Currents," in Physics of Quantum Electronics 7, Editors S.F. Jacobs, H.S. Pilloff, M. Sargeant, M.O. Scully, and R. Spitzer, (Addison-Wesley, Reading, Mass., 1980), p. 377.
5. See for example, P. Sprangle and C.M. Tang, Appl. Phys. Lett. 39, 677 (1981), or J. Elliott, "Optical Mode Control in the Free-Electron Laser," in Physics of Quantum Electronics 8, Editors S.F. Jacobs, G.T. Moore, H.S. Pilloff, M. Sargent, M.O. Scully, and R. Spitzer, (Addison-Wesley, Reading, Mass., 1982), p. 531.
6. J.M. Slater and D.D. Lowenthal, J. Appl. Phys. 52, 44 (1981).
7. J.M. Slater, IEEE J. Quantum Electron. QE-17, 1476 (1981).
8. D.B. Rensch, Appl. Opt. 13, 2546 (1974).

9. A.E. Siegman, An Introduction to Lasers and Masers, (McGraw-Hill, New York, 1971), p. 305-330.
10. R.D. Richtmyer and K.W. Morton, Difference Methods for Initial Value Problems, (Interscience, New York, 1967), 2nd Ed., pp. 198-201.
11. M.R. Siegrist, M.R. Green, P.D. Morgan, and R.L. Watterson, Appl. Opt. 19, 3824 (1980).
12. J.P. Blewett and R. Chasman, J. Appl. Phys. 48, 2692 (1977).
13. M. Born and E. Wolf, Principles of Optics, (Pergamon, Oxford, 1970), 4th Ed., pp. 463-464.

**END**

**FILMED**

**6-83**

**DTIC**